Mutual Orbit Orientations of Transneptunian Binaries

W.M. Grundy[1,2], K.S. Noll[3], H.G. Roe[4], M.W. Buie[5], S.B. Porter[5], A.H. Parker[5], D. Nesvorný[5], H.F. Levison[5], S.D. Benecchi[6], D.C. Stephens[7], and C.A. Trujillo[2]

1. Lowell Observatory, Flagstaff Arizona.
2. Northern Arizona University, Flagstaff Arizona.
3. NASA Goddard Space Flight Center, Greenbelt Maryland.
4. Gemini Observatory/AURA, Santiago Chile.
5. Southwest Research Institute, Boulder Colorado.
6. Planetary Science Institute, Tucson Arizona.
7. Brigham Young University, Provo Utah.

— Published in 2019 in *Icarus* **334,** 62-78; DOI:10.1016/j.icarus.2019.03.035 —

Abstract

We present Keplerian orbit solutions for the mutual orbits of 17 transneptunian binary systems (TNBs). For ten of them, the orbit had not previously been known: 60458 2000 CM_{114}, 119979 2002 WC_{19}, 160091 2000 OL_{67}, 160256 2002 PD_{149}, 469514 2003 QA_{91}, 469705 ǂKágára, 508788 2000 CQ_{114}, 508869 2002 VT_{130}, 1999 RT_{214}, and 2002 XH_{91}. Seven more are systems where the size, shape, and period of the orbit had been published, but new observations have now eliminated the sky plane mirror ambiguity in its orientation: 90482 Orcus, 120347 Salacia-Actaea, 1998 WW_{31}, 1999 OJ_4, 2000 QL_{251}, 2001 XR_{254}, and 2003 TJ_{58}. The dynamical masses we obtain from TNB mutual orbits can be combined with estimates of the objects' sizes from thermal observations or stellar occultations to estimate their bulk densities. The ǂKágára system is currently undergoing mutual events in which one component casts its shadow upon the other and/or obstructs the view of the other. Such events provide valuable opportunities for further

characterization of the system. Combining our new orbits with previously published orbits yields a sample of 35 binary orbits with known orientations that can provide important clues about the environment in which outer solar system planetesimals formed, as well as their subsequent evolutionary history. Among the relatively tight binaries, with semimajor axes less than about 5% of their Hill radii, prograde mutual orbits vastly outnumber retrograde orbits. This imbalance is not attributable to any known observational bias. We suggest that this distribution could be the signature of planetesimal formation through gravitational collapse of local density enhancements such as caused by the streaming instability. Wider binaries, with semimajor axes greater than 5% of their Hill radii, are somewhat more evenly distributed between prograde and retrograde orbits, but with mutual orbits that are aligned or anti-aligned with their heliocentric orbits. This pattern could perhaps result from Kozai-Lidov cycles coupled with tidal evolution eliminating high inclination wide binaries.

Introduction

Discovery of the first transneptunian object (TNO) in 1992 (Luu & Jewitt 1993) opened a whole new phase space for untangling the dynamical interactions of objects in our solar system. Some twenty-seven years later over 3000 such objects have been identified, more than half with well defined heliocentric orbits that can be dynamically classified into several main groups: Classical, Resonant, Scattered, and Centaurs (Elliot et al. 2005; Gladman et al. 2008). Classical objects have nearly circular orbits with low inclinations, Resonant objects occupy mean-motion resonances with Neptune. Scattered objects have been or are being perturbed by interactions with giant planets. Centaurs occupy orbits that extend into the giant planet zone and are thus especially rapidly perturbed. Within each of these groups additional sub-populations can be broken out.

The first binary TNO, identified in 2002 (Veillet et al. 2002) opened the door to our ability to obtain physical parameters such as size and density. Subsequent high spatial resolution imaging has discovered more than 80 such systems, indicating that many TNOs are binaries or multiple systems (e.g., Noll et al. 2008). Transneptunian binaries (TNBs) provide a valuable opportunity for more detailed remote characterization of a sample of the Kuiper belt population. Accurate masses can be determined from their mutual orbits, and can be combined with size estimates to constrain bulk densities. The statistical distributions of separations, eccentricities,

and orientations of binary orbits contain clues about the protoplanetary disk environment in which they formed (e.g., Goldreich et al. 2002; Weidenschilling 2002; Funato et al. 2004; Astakhov et al. 2005; Nazzario et al. 2007; Nesvorný et al. 2010; Kominami et al. 2011). TNB orbits are also influenced by post-formation processes, including collisions or close encounters with 3rd bodies (e.g., Petit & Mousis 2004; Nesvorný et al. 2011; Parker et al. 2011), and solar tide perturbations (e.g., Kozai 1962; Lidov 1962), potentially in concert with tidal evolution (e.g., Perets & Naoz 2009; Naoz et al. 2010; Fang & Margot 2012; Porter & Grundy 2012). To tease apart the threads of the various influences on TNB mutual orbits requires a large sample of known orbits. We have been working for more than a decade to build such a sample by observing the relative positions of TNB components as they change over time to determine the mutual orbits of as many as we can.

This paper reports new observations and orbit solutions for seventeen transneptunian binaries, with orbits now fully determined for thirteen of them. Among these binary systems, two are especially interesting because the dynamical masses from their mutual orbits can be combined with published constraints on their sizes to estimate their bulk densities. Additionally, one of the systems is currently undergoing mutual events. The growing sample of known TNB mutual orbits shows intriguing patterns in their inclinations with respect to the bodies' heliocentric orbits that can provide constraints on planetesimal and binary formation mechanisms.

Data sources and processing

Resolving the very faint and closely spaced components of TNB systems requires high spatial resolution coupled with high sensitivity. When numerous binaries first began to be discovered in the Kuiper belt in the early 2000s, the Hubble Space Telescope (HST) was the only facility that could provide useful relative astrometry, owing to its diffraction-limited image quality, exceptionally stable pointspread function (PSF), and the low sky background from its vantage point above Earth's atmosphere. Subsequently, laser guide star adaptive optics systems have become an additional valuable source of data. This section will briefly describe all of the facilities and instruments we used to collect data for this paper, along with instrument-specific details of data processing. In many cases, the binary was first discovered using one HST instrument and then subsequently observed using others as well as ground-based facilities. The

result tends to be a data set that is highly heterogeneous in terms of the formal and systematic uncertainties associated with the various epochs.

We begin with the HST data. These resulted from numerous separate observing programs extending from 2001 through 2015, led by various investigators using different instruments in pursuit of a great variety of scientific goals. For all HST instruments, Tiny Tim model PSFs (Krist et al. 2011) were fitted to the images. The premier HST instrument for TNB studies was the High Resolution Camera (HRC) of the Advanced Camera for Surveys (ACS; Sirianni et al. 2005), thanks to its sensitivity and fine pixel scale that sampled the pointspread function (PSF) of the telescope reasonably well. Nine of the seventeen TNB systems for which new data are presented in this paper were discovered to be binaries using ACS HRC. Prior to the installation of ACS during servicing mission 3B in 2002, as well as after its untimely failure in 2006, the workhorse instrument for TNB studies was the Wide Field Planetary Camera 2 (WFPC2; McMaster et al. 2008; Dolphin 2009). Servicing mission 4 in 2009 replaced WFPC2 with the more modern Wide Field Camera 3 (WFC3; Bellini et al. 2011). Two observations with the Near Infrared Camera and Multi-Object Spectrometer (NICMOS; Skinner et al. 1998; Schultz et al. 2003) were also used in our analysis, though the NIC2 camera used for those observations offers lower spatial resolution than the visible wavelength instruments, with a pixel scale of 75 mas, and the diffraction limit is worse at near infrared wavelengths than it is in the visible. Nominal Tiny Tim focus values were used for most HST instruments, but for WFC3 we used the model focus history that accounts for telescope breathing. More details on our processing of HST observations of TNBs can be found in a series of earlier publications (Grundy et al. 2008, 2009, 2011, 2012, 2014, 2015)

Laser guide star adaptive optics (LGS AO) systems on the largest ground-based telescopes can contribute valuable data, too. New observations from the 8 m single mirror Gemini North telescope and from the 10 m segmented mirror Keck 2 telescope are reported in this paper. LGS AO observations with these facilities are subject to three important limitations. First, both telescopes are located on the summit of Mauna Kea, in Hawai'i, limiting their ability to observe TNBs at southerly latitudes. Second, the AO systems work at near infrared wavelengths where night sky emission is relatively bright, limiting the sensitivity so only brighter TNB systems can be usefully observed. Third, almost all TNBs are too faint for the target itself to be usable for tip-tilt correction, so they can only be observed using LGS AO when they pass near a brighter

appulse star that can be used as a tip-tilt reference. For Keck 2, approximate limits for these stars are Johnson *R* magnitude brighter than 17 within ~60 arcsec of the TNB target, while at Gemini North, they are $R < 16$ at a separation below ~25 arcsec. This project was awarded Keck time through a series of single-semester proposals to the NASA TAC. The observations were done using the NIRC2 camera (Le Mignant et al. 2006) on the Keck 2 telescope. For Gemini, our time allocation resulted from NOAO survey program 11A-0017 which ran from 2011 to 2013, using the NIRI camera (Hodapp et al. 2003) with the ALTAIR (Herriot et al. 2000) adaptive optics system. For both NIRI and NIRC2, PSF fitting of primary and secondary was done using the same PSF for primary and secondary, differing only in location and intensity. Circularly symmetric Gaussian or Lorentzian functional forms were used to fit most images, but in a few cases, elliptical PSFs were needed. More details on our processing of LGS AO observations of TNBs can be found in Grundy et al. (2015).

Our usual method of estimating astrometric uncertainties was to record multiple images at a given epoch and to measure positions in each image. The astrometric uncertainty for that visit was then estimated from the scatter among the single-frame measurements. We occasionally imposed an uncertainty floor based on experience with the various instruments for targets in the same general brightness range. This was mostly done in cases where relatively few frames were obtained.

The resulting astrometric data appear in Table 1. These data include published observations for the seven systems where orbits were previously published. Our numbers in Table 1 may not be identical to the previously published numbers, since observations were re-reduced using our current software tools so as to have as consistent as possible of a data set for orbit fitting. Photometry from these observations will be considered in a separate paper. A machine-readable version of the table is provided as supplementary material.

Typesetter: Please place Table 1 somewhere near here.

Orbit fitting procedures

We pursue orbit determination through two distinct stages. During the first stage, the orbit is not yet known. We use Monte Carlo techniques to sample the probability distribution in orbital element space to determine when the orbit is sufficiently well known to proceed to the next stage of orbit fitting (Grundy et al. 2008). For systems where primary and secondary are almost the

same brightness and thus indistinguishable from one another, we also randomize the identities in each observational epoch, to ensure that all possible solutions are sampled. As a result, these cases require more observations to resolve (e.g., Grundy et al. 2012).

When the orbital element sampling shows that only a single solution is possible for the period, semimajor axis, eccentricity, we transition to an orbit fitting scheme. In cases where the primary and secondary have near equal brightnesses, we also require all but one permutation of primary versus secondary identities to be excluded. For orbit fitting, we use the downhill simplex "amoeba" algorithm (Nelder & Mead 1965; Press et al. 1992) to iteratively adjust the Keplerian orbital elements to minimize the χ^2 statistic between observations and computed positions. This step is repeated for 1000 versions of the astrometry, each randomized according to the astrometric uncertainties, to obtain 1000 orbit solutions that capture the probability distribution for each of the fitted orbital elements. The standard deviation around each element is reported as a 1-σ error bar, but the solution clouds can be provided on request. Considering the heterogeneity of the data, with observations from many different instruments obtained over many years, we closely consider the residuals to look for potential discrepancies in which one instrument or epoch is inconsistent with the others and should be rejected or have its uncertainty inflated. Overall, we find that the different instruments tend to produce reasonably consistent results.

New Transneptunian Binary System Orbits

In this section we step through the 17 systems presenting our new data and orbit solutions and describing details specific to the individual systems. Readers more interested in the ensemble results may wish to skip ahead to the following section.

60458 2000 CM_{114}

This object was discovered at the 4 meter Mayall telescope at Kitt Peak (Millis et al. 2000). It orbits the Sun in an eccentric ($<e_\odot> = 0.4$, averaged over a 10 Myr integration) and inclined ($<i_\odot> = 22°$) orbit that is classified as part of the scattered disk by the Deep Ecliptic Survey (e.g., Elliot et al. 2005) and as a detached object according to the Gladman et al. (2008) nomenclature. The companion, about 0.6 mags fainter than the primary, was discovered using HST ACS HRC (Noll et al. 2006a). Initial follow-up observations using HST WFPC2 failed to determine a

unique orbit, but two additional HST observations with WFC3 UVIS were able to secure the near-circular prograde orbit in Table 2 with a period of 24.8254 ± 0.0013 days and semimajor axis 2497 ± 25 km.

90482 Orcus

The dwarf planet Orcus was discovered at Palomar observatory in 2004 by M.E. Brown, C.A. Trujillo, and D. Rabinowitz, and provisionally designated as 2004 DW. It orbits the Sun at a mean distance of 39.5 AU, in the 3:2 mean motion resonance with Neptune (e.g., Elliot et al. 2005; Gladman et al. 2008). The satellite Vanth, about 2.6 mags fainter than Orcus, was discovered in Hubble Space Telescope observations from 2005 (Brown and Suer 2007). Orbit solutions were published in several papers (e.g., Brown et al. 2010; Carry et al. 2011) but owing to the orientation of the orbit, viewed nearly face-on, it was initially difficult to resolve the sky-plane mirror ambiguity. A ground based LGS AO observation from Keck observatory in 2015 broke the ambiguity, showing the orbit to be retrograde (see Table 3).

119979 2002 WC_{19}

This object was discovered by Trujillo et al. (2003). It orbits the Sun at a mean distance of 47.8 AU, in the 2:1 mean motion resonance with Neptune (e.g., Elliot et al. 2005; Gladman et al. 2008). The companion, about 3 mag fainter than the primary, was discovered using HST ACS HRC (Noll et al. 2007a). Subsequent observations using HST WFPC2 and WFC3-UVIS, as well as ground-based LGS AO observations with Keck 2 NIRC2 revealed the orbit period to be 8.402 ± 0.0012 days and the semimajor axis to be 4091 ± 95 km (see Table 4). The mirror ambiguity has not yet been eliminated, so a prograde and a retrograde solution are both consistent with the data. The above period and semimajor axis figures and their uncertainties encompass both solutions.

120347 Salacia – Actaea

Salacia is a large, dwarf-planet sized TNO, discovered by Roe et al. (2005). With its relatively high inclination ($<i_{\odot}> = 25.6°$), it can be classified as a member of the extended scattered disk according to the Deep Ecliptic Survey nomenclature (e.g., Elliot et al. 2005), or of the Hot Classical population, according to the Gladman et al. (2008) nomenclature. Actaea,

about 2.4 mag fainter than Salacia, was discovered in HST ACS HRC images (Noll et al. 2006c). Subsequent observations using HST WFPC2 and Keck 2 NIRC2 enabled determination of the period, eccentricity, and semimajor axis published by Stansberry et al. (2012). New observations with Gemini NIRI and Keck 2 NIRC2 have now broken the mirror ambiguity, revealing that the orbit is prograde with a period of 5.493882 ± 0.000023 days and semimajor axis of 5724 ± 27 km (see Table 5). The very high value of chi-squared (χ^2 = 52, based on observations at 14 epochs) indicates potential problems, since a smaller value of 43.6 would indicate an orbit solution that can be excluded at 3 σ confidence. A plausible explanation could be that one or more of the astrometric observations or associated uncertainties are faulty, although there is not an obvious culprit in terms of unexpectedly large residuals. Another possibility is that an as-yet undiscovered third body could be present, perturbing the Salcacea-Actaea mutual orbit. Or, the orbit of Actaea could be precessing, due to the non-spherical shape of Salacea.

Our updated system mass of (4.922 ± 0.071) × 10^{20} kg can be combined with estimates of the sizes of Salacia and Actaea to refine the bulk density of the system. From thermal observations, the projected area of Salacia plus Actaea corresponds to a sphere of diameter 901 ± 45 km (Vilenius et al. 2012), 874 ± 32 km (Fornasier et al. 2013), or 914 ± 39 km (Brown & Butler 2017). Combining these three independent measurements yields an effective diameter of 893 ± 22 km. Assuming the two bodies share the same albedo and that both are spheres, their 2.37 ± 0.06 mag difference in brightness (Stansberry et al. 2012) implies diameters of 846 ± 21 and 284 ± 10 km for Salacia and Actaea, respectively. We can then calculate their average bulk density to be 1.50 ± 0.12, somewhat higher than the density calculated by Brown & Butler (2017), due to the combination of a higher mass with a smaller volume. Of course, having assumed spherical shapes and equal albedos limits the value of this calculation.

160091 2000 OL_{67}

This object was discovered by the Deep Ecliptic Survey team (Buie et al. 2000). With its small heliocentric eccentricity and inclination ($\langle i_\odot \rangle$ = 3.49°, $\langle e_\odot \rangle$ = 0.106) it can be classified as a Cold Classical TNO (e.g., Elliot et al. 2005; Gladman et al. 2008). The companion, about 0.6 mag fainter than the primary, was discovered in 2007 in images obtained with HST WFPC2 (Marchis et al. 2007). Subsequent follow-up observations were done using Keck 2 NIRC2 (4 epochs) and Gemini NIRI (2 epochs). The orbit period is 347.14 ± 0.43 days and semimajor axis

is 7830 ± 550 km (see Table 6). The mirror ambiguity has not yet been eliminated, so a prograde and a retrograde solution are both consistent with the data. The above period and semimajor axis figures and their uncertainties encompass both solutions.

160256 2002 PD_{149}

This object was discovered by the Deep Ecliptic Survey team. With its small heliocentric eccentricity and inclination ($<i_{\odot}>$ = 3.30°, $<e_{\odot}>$ = 0.067) it can be classified as a Cold Classical TNO (.g., Elliot et al. 2005; Gladman et al. 2008). A widely separate companion, about 0.4 mag fainter than the primary, was discovered with HST WFPC2 (Noll et al. 2007b). Subsequent follow-up observations were done with ground-based LGS AO using Gemini NIRI (1 epoch) and Keck 2 NIRC2 (3 epochs). They reveal that the mutual orbit is prograde with a period of 1675.5 ± 3.2 days and a semimajor axis of 26780 ± 340 km (see Table 7).

469514 2003 QA_{91}

This object was discovered by the Deep Ecliptic Survey team (Wasserman et al. 2004). With its small heliocentric eccentricity and inclination ($<i_{\odot}>$ = 1.04°, $<e_{\odot}>$ = 0.077) it can be classified as a Cold Classical TNO (.g., Elliot et al. 2005; Gladman et al. 2008). The near-equal brightness companion was discovered using HST ACS HRC (Noll et al. 2008). Subsequent observations using HST WFC3 and Keck 2 NIRC2 reveal that the mutual orbit period is 10.10890 ± 0.00026 days and semimajor axis is 1595 ± 45 km (see Table 8), currently oriented nearly face-on toward the inner solar system. The mirror ambiguity has not yet been resolved, so a prograde and a retrograde solution are both consistent with the data, both highly inclined to the heliocentric orbit plane. The above period and semimajor axis figures and their uncertainties encompass both solutions. Although the best fit eccentricity values for the two orbits are not exactly zero, the orbit is likely to be circular. Small non-zero eccentricities tend to be associated with noise and uneven longitude sampling in the astrometric data.

469705 ǂKǻgára

Transneptunian object ǂKǻgára[1] was discovered by the Deep Ecliptic Survey team and

1 The names have been proposed to the International Astronomical Union's Small Bodies Nomenclature Committee. In the mythology of the ǀXam people of the Kalahari desert in South Africa, ǂKǻgára and his brother in law !Hãunu fight an epic battle in the east using thunder and lightning, producing mountainous clouds and

provisionally designated as 2005 EF_{298} (Buie et al. 2005). With its small heliocentric orbital inclination and eccentricity ($<i_{\odot}>$ = 1.60°, $<e_{\odot}>$ = 0.085) it can be considered a Cold Classical TNO (e.g., Elliot et al. 2005; Gladman et al. 2008). Its mean distance from the Sun of 44.1 AU further suggests that it could belong to the Petit et al. (2011) "kernel" sub-component of the Cold Classical population. The satellite !Hãunu was discovered in 2009 using HST WFPC2 observations (Noll et al. 2009). Subsequent follow-up observations with HST WFC3 and ground-based LGS AO observations with Gemini NIRI (2 epochs) and Keck 2 NIRC2 (1 epoch) revealed the orbit to be prograde with a 128.107 ± 0.027 day period and a 7670 ± 140 km semimajor axis (see Table 9).

Our updated system mass of (2.18 ± 0.12) × 10^{18} kg can be combined with constraints on the sizes of ǂKágára and !Hãunu to estimate the bulk density of the system. Thermal infrared observations obtained with the Herschel space telescope were used to derive a projected surface area corresponding to that of a sphere with a diameter of 174^{+27}_{-32} km (Vilenius et al. 2012). Again assuming both components share the same albedo, we can use the 0.59 mag difference in brightness (Noll et al. 2009) to divide that surface area between spheres of diameter 138^{+21}_{-25} and 122^{+16}_{-19} km, for ǂKágára and !Hãunu, respectively. We can then calculate their average bulk density to be $1.1^{+0.9}_{-0.4}$ g cm^{-3}. This is not a particularly constraining density, consistent with the low densities reported for other small, Cold Classical TNBs, as well as the higher densities reported for larger TNBs in more excited dynamical populations (e.g., Brown et al. 2010; Stansberry et al. 2012; Vilenius et al. 2012; Brown 2013a, 2013b; Vilenius et al. 2014; Grundy et al. 2015; Brown & Butler 2017).

An interesting feature of the ǂKágára - !Hãunu orbit is that its orientation is currently nearly edge-on, as seen from the inner solar system. This configuration produces mutual events in which the two bodies alternate in transiting one another as seen from Earth (occultation events)

---

rain. The conflict was over ǂKágára returning his younger sister, !Hãunu's wife, to their parents. The ǀXam language is no longer spoken, but the language and culture were documented by Wilhelm and Dorothea Bleek and Lucy Lloyd working with a series of ǀXam informants between 1870 and 1884. The story of ǂKágára and !Hãunu was told to them by ǀHankass'o. The ǀXam language motto on South Africa's national coat of arms is "!ke e: ǀxarra ǁke", meaning "diverse people unite." In ǀXam orthography, ǀ, ǁ, ǂ, and ! represent dental, lateral, palatal, and (post)aveolar clicks, respectively. Recordings are available at http://www2.lowell.edu/~grundy/tnbs/469705_how_to_say.html.

and/or casting shadows upon one another (eclipse events). If the two bodies are spheres of the sizes mentioned earlier, on the orbit we report, then the mutual events began in 2015 and will continue through 2035. In general, there are two mutual event opportunities per 128 day orbital period, but not all events involve both eclipse and occultation components, due to the motion of the Earth around the Sun. We anticipate approximately 70 events in total, though not all will be suitable for Earth-based observations, such as when Earth and ǂKágára are on opposite sides of the Sun. Events early and late in the season tend to be shallow ones, while those near the middle of the season are deeper.

The 0.694 ± 0.013 eccentricity of the orbit has a significant influence on the events. "Inferior" events, in which !Hãunu is in front of ǂKágára as seen from Earth, nearly coincide with apoapse. At that time, the orbital motion is comparatively slow, so these events are much longer in duration than "superior" events where ǂKágára is in front. Where superior events can last as long as 8 hours, inferior events can go on for more than two days between first and last contact. The greater separation around apoapse also results in a shorter season for inferior events. Superior events run from 2015 through 2035, but inferior events only run from 2022 through 2027. Another consequence of the wide orbital separation at the time of inferior events is that the eclipse and occultation components can be widely separated in time. Close to opposition, this temporal separation is minimized, with the two components combining to produce slightly longer events, but away from opposition, the temporal separation can grow to be longer than the duration of individual events, resulting in adjacent pairs of events.

Mutual events provide a valuable opportunity to constrain the properties of the component bodies of the system, if they can be observed with suitable instrumentation. But timing uncertainties for events over the coming decade are substantial due to the combination of the present-day orbital longitude uncertainty plus a contribution from the orbital period uncertainty that grows monotonically over time. Already for events in 2019, the 1-σ timing uncertainty is ±13 hours, and as of the mid-season in 2025, it will have grown to ±24 hours. Additional observations will be crucial for refining the orbit to the point where events can be predicted with sufficient precision for observers to be able to pursue telescope time for them.

508788 2000 CQ_{114}

This object was discovered by the Deep Ecliptic Survey team. With its small heliocentric orbital inclination and eccentricity ($\langle i_{\odot} \rangle = 2.2°$, $\langle e_{\odot} \rangle = 0.12$), this object is a Cold Classical

TNO (e.g., Elliot et al. 2005; Gladman et al. 2008). The near-equal brightness companion was discovered in 2003 using HST NICMOS (Stephens et al. 2004). Subsequent follow-up observations using HST WFPC2 and WFC3 reveal the orbit to be prograde, with a 220.478 ± 0.045 day period and a 6940 ± 32 km semimajor axis (see Table 10).

508869 2002 VT_{130}

This object was discovered by the Deep Ecliptic Survey team (Millis et al. 1999). Its small heliocentric orbital inclination and eccentricity ($<i_{\odot}>$ = 2.78°, $<e_{\odot}>$ = 0.034) make it a Cold Classical TNO (e.g., Elliot et al. 2005; Gladman et al. 2008). The companion, about 0.4 mags fainter than the primary, was discovered in 2008 using HST WFPC2 (Noll et al. 2009). Subsequent ground-based LGS AO follow-up observations with Gemini NIRI (2 epochs) and Keck 2 NIRC2 (3 epochs) revealed the mutual orbit to have a 30.7615 ± 0.0064 day period and a 3026 ± 90 km semimajor axis (see Table 11). The mirror ambiguity has not yet been eliminated, so prograde and retrograde solutions are both consistent with the data. The above period and semimajor axis figures and their uncertainties encompass both solutions.

1998 WW_{31}

This object was discovered by the Deep Ecliptic Survey team. With heliocentric mean eccentricity 0.085 and inclination 8.34°, 1998 WW_{31} can be classified as a Hot Classical TNO (e.g., Elliot et al. 2005; Gladman et al. 2008). The 0.4 mag fainter, and widely separated companion was discovered in CFHT images (Veillet et al. 2002) taking pride of place as the first new TNB to be discovered since Pluto-Charon, and presaging a whole new field of TNB studies. Veillet et al. (2002) published an orbit based on HST WFPC2 observations as well as ground-based observations. Their astrometric measurements were not included in the paper, so we could not duplicate their orbit solution or check if the mirror ambiguous solution could be formally excluded according to our criteria. Using our data reduction procedures, we re-reduced the data from HST programs 9259, 9320, and 9508, all of which were obtained with WFPC2 between 2001 and 2003. A decade later, a pair of LGS AO observations using Gemini NIRI and Keck 2 NIRC2 provided a substantial parallax enabling us to confidently rule out the mirror solution, yielding the prograde orbit in Table 12 with 587.27 ± 0.17 day period and 22617 ± 47 km semimajor axis. The eccentricity is unusually high for a TNB at 0.8193 ± 0.0020.

1999 OJ_4

Transneptunian object 1999 OJ_4 was discovered by Kavelaars et al. (1999). With heliocentric mean eccentricity 0.018 and inclination 2.58°, this object would be considered a Cold Classical TNO, except that its mean semimajor axis of 38.1 AU lies closer to the Sun than the 2:3 mean motion resonance with Neptune, often considered to be the inner bound of the Classical belt (e.g., Elliot et al. 2005; Gladman et al. 2008). Whether such objects should be considered as members of an Inner Classical belt or something else is not yet settled. The near-equal brightness companion was discovered in HST NICMOS images obtained in 2002 (Stephens & Noll 2006). An orbit solution published by Grundy et al. (2009), provided the period, semimajor axis, and eccentricity but did not break the mirror ambiguity. Subsequent LGS AO observations with NIRI and NIRC2 now reveal that the prograde orbit solution is the correct one, with 84.1147 ± 0.0050 day period and 3306 ± 17 km semimajor axis (see Table 13).

1999 RT_{214}

Transneptunian object 1999 RT_{214} was discovered by Trujillo et al. (1999). It has a small heliocentric orbital inclination and eccentricity ($\langle i_\odot \rangle$ = 2.77°, $\langle e_\odot \rangle$ = 0.059) and can thus be considered a Cold Classical TNO (e.g., Elliot et al. 2005; Gladman et al. 2008). The companion, about 1 mag fainter than the primary, was discovered in HST ACS HRC images obtained in 2006 (Noll et al. 2006d). Subsequent observations using HST WFPC2 and WFC3 as well as a ground-based LGS AO observation with Keck 2 NIRC2 show that the orbit is prograde, with a 126.504 ± 0.046 day period and a 3396 ± 66 km semimajor axis (see Table 14).

2000 QL_{251}

This object was discovered by the Deep Ecliptic Survey team (Wasserman et al. 2001). It orbits the Sun at a mean distance of 47.8 AU, in the 2:1 mean motion resonance with Neptune (e.g., Elliot et al. 2005; Gladman et al. 2008). The near-equal brightness companion was discovered in an HST ACS HRC observation from 2006 (Noll et al. 2006b). Subsequent HST observations with WFPC2 and WFC3 were used to obtain the period, semimajor axis, and eccentricity (Grundy et al. 2009), but the data at the time of that publication were insufficient to break the mirror ambiguity. Subsequent ground-based LGS AO observations with NIRI and NIRC2 reveal that the retrograde orbit solution is the correct one, with a 56.4495 ± 0.0039 day

period and a 4992 ± 16 km semimajor axis (see Table 15).

2001 XR_{254}

This object was discovered using the Canada France Hawaii 3.6 m and University of Hawaii 2.2 m telescopes on Mauna Kea (Jewitt et al. 2002). Its low inclination ($<i_{\odot}> = 2.7°$) and low eccentricity ($<e_{\odot}> = 0.024$) heliocentric orbit make it a Cold Classical object (e.g., Elliot et al. 2005; Gladman et al. 2008). The companion, about 0.4 mag fainter than the primary, was discovered using HST ACS HRC (Noll et al. 2008). From follow-up observations using HST WFPC2, a mirror-ambiguous orbit was published by Grundy et al. (2009). A subsequent Keck LGS AO observation broke the mirror ambiguity, leading to the prograde, eccentric orbit in Table 16 with a 125.579 ± 0.048 day period and 9311 ± 52 km semimajor axis.

2002 XH_{91}

Transneptunian object 2002 XH_{91} was discovered by the Deep Ecliptic Survey team (Wasserman et al. 2003). With its small heliocentric orbital inclination and eccentricity ($<i_{\odot}> = 3.0°$, $<e_{\odot}> = 0.08$) it can be classified as a Cold Classical TNO (e.g., Elliot et al. 2005; Gladman et al. 2008). Its mean distance from the Sun of 44.0 AU suggests that it could belong to the Petit et al. (2011) "kernel" sub-component of the Cold Classical population. The widely-separated companion, about 1 mag fainter than the primary, was discovered using HST WFPC2 (Noll et al. 2009). Subsequent ground-based LGS AO observations with Gemini NIRI (2 epochs) and Keck 2 NIRC2 (2 epochs) enabled the determination of the prograde orbit in Table 17 with 371.15 ± 0.17 day period and 22430 ± 410 km semimajor axis.

2003 TJ_{58}

Transneptunian object 2003 TJ_{58} was discovered by the Canada-France Ecliptic Plane Survey (CFEPS) team (Kavelaars et al. 2009). With its small heliocentric orbital inclination and eccentricity ($<i_{\odot}> = 1.3°$, $<e_{\odot}> = 0.09$) it can be classified as a Cold Classical TNO (e.g., Elliot et al. 2005; Gladman et al. 2008). The companion, about 0.5 mag fainter than the primary, was discovered using HST ACS HRC images from 2006 (Noll et al. 2008). Subsequent observations during 2007 with HST WFPC2 were used to obtain the period, semimajor axis, and eccentricity (Grundy et al. 2009). One more visit in 2014 with HST WFC3 UVIS was sufficient to break the

mirror ambiguity, resulting in the prograde orbit in Table 18 with a 137.682 ± 0.034 day period and a 3834 ± 50 km semimajor axis.

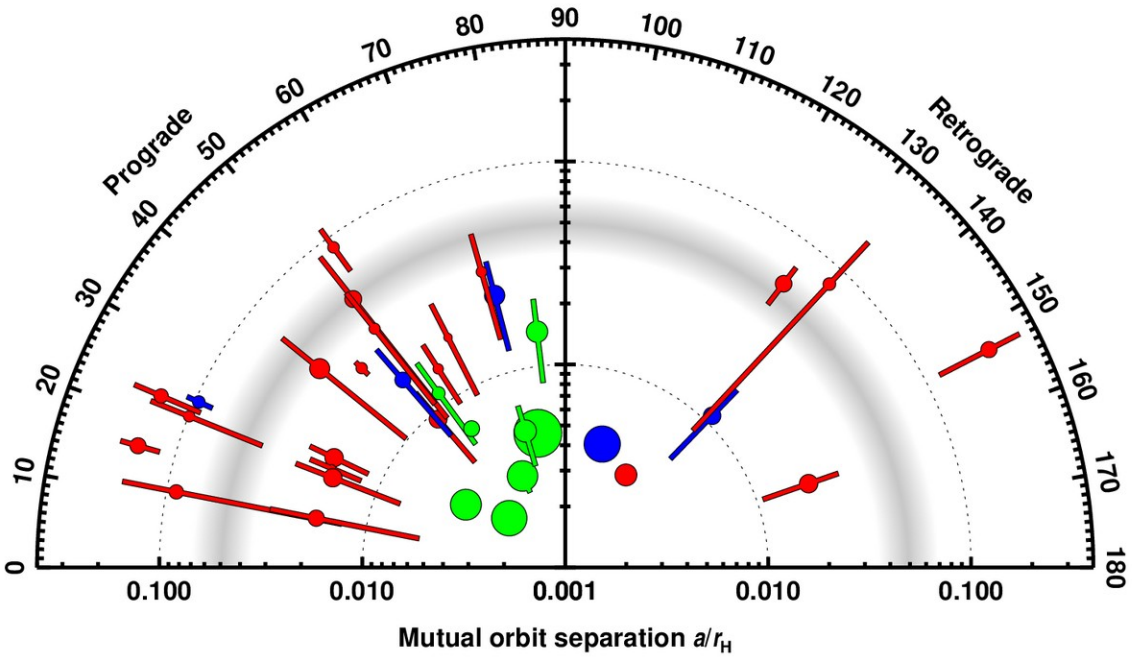

Fig. 1. Binary mutual orbit inclination versus semimajor axis. Symbol sizes are indicative of system mass. In the on-line version, colors indicate dynamical class with red for Classical TNOs, blue for resonant TNOs, green for Centaurs and scattered disk objects, following Elliott et al. (2005). Radial bars indicate eccentricity, extending from periapse to apoapse. A fuzzy gray arc indicates the ~0.05 r_H separation where there appears to be a transition between tight and wide binaries with distinct orientation distributions.

Orbit Orientations

This paper provides new mutual orbit orientation information for 13 TNB systems. We can combine these new orientations with 22 previously-published orbits to obtain a sample of 35, giving a more complete picture of the distribution of orbital orientations for TNBs. The combined list appears in Table 19, along with a further 11 where the orbit orientation is not yet resolved.

Typesetter: Please place Table 19 somewhere near here.

The azimuthal axis of Fig. 1 shows the mutual orbit inclination relative to each object's heliocentric orbit plane. The mutual orbit semimajor axis, as well as periapse and apoapse

separations, are indicated along the radial axis, expressed in units of the Hill radius r_H, computed at perihelion as

$$r_H = a_\odot(1-e_\odot)\left(\frac{M_{sys}}{3M_\odot}\right)^{\frac{1}{3}} , \qquad \text{Equation 1}$$

where $a_\odot$ and $e_\odot$ are the heliocentric orbit semimajor axis and eccentricity and $M_\odot$ is the mass of the Sun. It is immediately obvious from this figure that there are more prograde TNB orbits than retrograde ones.

The distribution of orbital inclinations can be compared to a random distribution by plotting both distributions as cumulative curves, as in Fig. 2. The Kuiper statistic (e.g., Press et al. 1992) can be used to test the probability of the observed sample of orbit orientations having been drawn from a random distribution. That probability is 0.08%, meaning that a random distribution can be excluded with 3.4 σ confidence. Another way to look at the observed asymmetry is to compare with a simple binary choice: what are the odds of getting 7 or fewer heads in 35 coin tosses? The answer, from binomial statistics, is 0.025%.

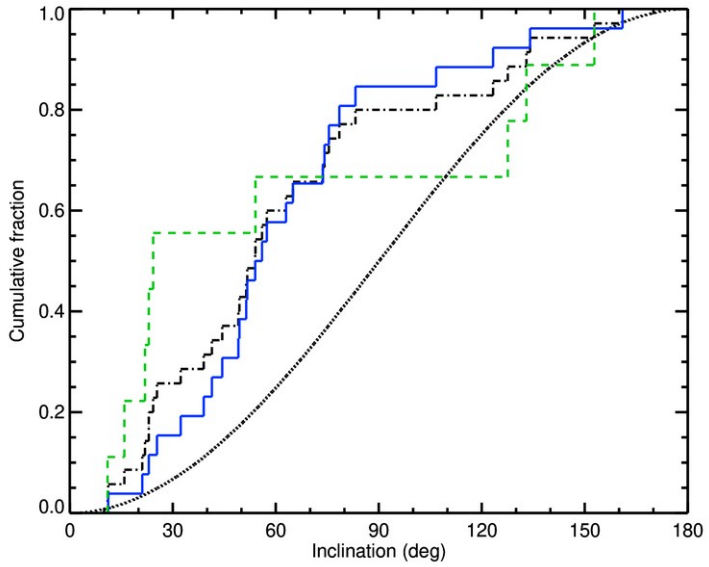

Fig. 2. Comparison of observed orientations with the cumulative distribution of inclinations for randomly oriented orbits (smooth dotted curve). The dot-dash curve is for all binaries, the dashed curve is for only the wide binaries with $a/r_H > 0.05$ (green in the on-line version), and the solid (blue) curve is for only tight binaries with $a/r_H < 0.05$.

Parker et al. (2011) studied a sample of seven wide TNBs of which four had prograde and three had retrograde orbits. The sample of wider binaries, those with a/r_H greater than roughly 0.05, has now expanded to nine, of which six are prograde. With a third of the wide binary orbits being retrograde, they appear to have somewhat more balanced numbers than the tighter binaries

with $a/r_H < 0.05$, where only four out of twenty six are retrograde. It should be noted that the precise location and nature of the transition are not clearly determined by our data. It is also unclear if this trend holds for all dynamical classes. Brunini (2019) show that encounters with giant planets can flip TNB orbits from prograde to retrograde or vice versa. The objects in our sample most likely to have encountered giant planets are the scattered disk TNBs and Centaurs, but all eight of these objects in our sample have prograde mutual orbits, as do the majority of the Classical TNBs. Of the five resonant TNBs, three are prograde and two are retrograde, consistent with a random distribution, though the sample of TNBs in resonances is small.

Among the nine wide binaries, none are highly inclined with respect to their heliocentric orbits. The absence of highly inclined orbits among wide binaries was also first reported by Parker et al. (2011) and could be a natural consequence of the effect of the Sun's gravity. Solar tides causes oscillation of the binary orbit eccentricity and inclination relative to the heliocentric orbit, preserving the constant $\sqrt{1-e^2}\cos(i)$ (Kozai 1962; Lidov 1962). More inclined orbits oscillate with greater amplitude, and high inclination orbits can reach extremely high eccentricity. The wide separation at apoapse during eccentricity extremes in Kozai-Lidov oscillating TNBs may enable flipping between prograde and retrograde orbit or even facilitate escape of the companion through encounters with third bodies. The eccentricity extremes can also promote tidal interactions during periapse that dissipate orbital energy resulting in tightening of the orbit, known as Kozai Cycles with Tidal Friction, or KCTF (e.g., Perets & Naoz 2009; Fang & Margot 2012). In modeling KCTF evolution of TNBs, Porter & Grundy (2012) found that many initially wide, high inclination TNBs evolve into TNBs with tight circular orbits. Consistent with this picture, the TNBs with circular orbits in our sample tend to be the tighter ones, and include a few with high inclinations, but relatively few of our Classical TNBs are among them. The orbits of tighter binaries are less influenced by Kozai-Lidov effects because quadrupole and higher order terms from the non-spherical shapes of small bodies become increasingly important at smaller separations. Nicholson et al. (2008) write the following equation for the critical separation a_{crit} where solar-induced precession and the effect of the J_2 component of the pimary's gravity field are balanced.

$$a_{crit} = \left(2 J_2 \frac{M_{sys}}{M_\odot} R_1^2 a_\odot^3 \right)^{\frac{1}{5}} , \qquad \text{Equation 2}$$

where R_1 is the primary's radius. At separations smaller than a_{crit}, J_2 controls the orbital

dynamics and Kozai-Lidov effects are comparatively unimportant.

To examine the distribution of inclinations relative to the heliocentric orbit, we fold the inclination distribution around 90°, so that low inclination prograde and retrograde orbits have small values and highly inclined orbits have large values. These folded inclination distributions are shown in Fig. 3. The inclinations of wide binaries are inconsistent with a random distribution in having a dearth of orbits with inclinations higher than 55°. The Kuiper statistic indicates the probability of this sample having been drawn from a random distribution as 2.6%. In contrast, the tight binaries look somewhat more consistent with a random distribution of inclinations, apart from the fact that they are overwhelmingly prograde, as we saw in Fig. 2. As with the transition from mostly prograde to more evenly distributed inclinations, the exact location and nature of the transition to avoidance of high inclinations among wider binaries is poorly characterized by the current sample. Both transitions appear to be in the vicinity of $a/r_H \approx 0.05$, but more data will be needed to test whether both occur at the same separation, and if the transitions are abrupt step-functions or are more gradual.

When discussing distributions of properties in a sample, it is important to consider potential biases in the construction of the sample. The most obvious bias is against tight binaries, because they are harder to discover in the first place, and it is harder to ascertain their mutual orbits. Our sample is certain to be strongly affected by this bias, with many tight binaries having been missed in searches for companions, or languishing on our list of known binaries that are still in need of further astrometry to secure their mutual orbits[2]. Some 37 known TNBs currently lack orbit solutions, while another 11 have the period, size, and shape of orbit determined, while the orientation remains ambiguous. If many of these orbits were retrograde, they could overturn the conclusions of this paper. But neither discovery nor subsequent orbit determination is sensitive to the sense of the orbital motion, so we do not believe the preponderance of prograde orbits among the tight binaries can be an effect of any sampling bias. There can be an effect from inclination, though: low inclination orbits are always seen near edge-on, whereas high inclination orbits can be viewed close to face-on, at least during parts of their heliocentric orbits. Face-on orbits are somewhat easier to secure, since epochs where the primary and secondary are too closely spaced to resolve are less probable. However, the one non-random effect we see in terms of the folded inclination distribution is the preference for low inclination orbits among the wide binaries, despite the fact that the low inclination orbits are the ones that are slightly harder to

2 Progress on orbit determination is tracked at http://www2.lowell.edu/~grundy/tnbs/.

determine. So if anything, correcting for this bias would make their non-random inclination distribution even stronger. However, we do not think this is an important correction to make, at least not for the wide binaries where we see the non-random distribution, since orbit determination is comparatively easy for wide binaries, even when the inclination is low. Correcting for this bias among the tight binaries would boost the number of low inclination orbits relative to that shown in Fig. 3. A potential related bias could arise if our sample favored objects north of the ecliptic plane, since they would be easier to observe from Mauna Kea's northern hemisphere location. But the distribution of current locations of our sample of 35 TNBs is symmetric around the ecliptic, with a median ecliptic latitude of −1° and standard deviation of 8°.

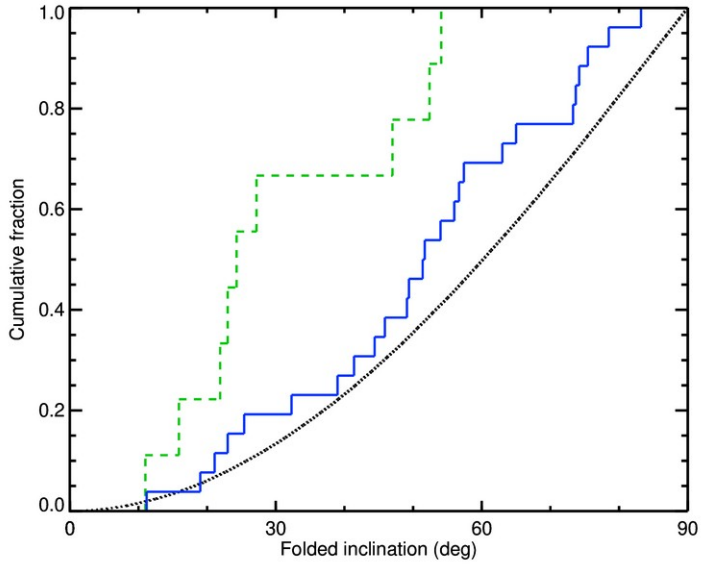

Fig. 3. Comparison of observed orientations with the folded distribution of inclinations for randomly oriented orbits (smooth dotted curve). The dashed curve is for only the wide binaries with $a/r_H > 0.05$ (green in the on-line version), and the solid (blue) curve is for only the tight binaries with $a/r_H < 0.05$.

Several binary formation models have been proposed. Most of these models assume that KBOs formed by hierarchical coagulation, where two-body collisions between objects in a dynamically cold protoplanetary disk lead to objects' accretion and growth (e.g., Shannon et al. 2016). They invoke collisions or collisionless interactions to produce capture of two KBOs on a bound binary orbit (e.g., Goldreich et al. 2002; Weidenschilling 2002; Funato et al. 2004; Astakhov et al. 2005; Lee et al. 2007; Kominami et al. 2011; Kominami & Makino 2014). For example, Goldreich et al. (2002) proposed that two KBOs can be captured during their encounter, assuming that a background sea of small planetesimals carries away the excess kinetic energy (the so-called L^2s model). Alternatively, capture can happen during a gravitational encounter of three bodies (L^3 in Goldreich et al. 2002).

A different kind of model of KBO binary formation has been suggested by Nesvorný et al. (2010). This model assumes that KBOs formed by a gravitational instability of the solid component of the protoplanetary disk, when collective effects generated collapse of solids into 100 km class objects. The streaming instability (Youdin & Goodman 2005) is probably the best candidate to trigger such a gravitational collapse (e.g., Simon et al. 2016, 2017), but other possibilities exist as well. Nesvorný et al. (2010) suggested that KBO binaries form during the gravitational collapse when the excess of angular momentum prevents the agglomeration of available mass into a solitary object. By modeling this process, they found that the gravitational collapse is capable of producing up to 100% binary fraction and correlated colors of binary components (Benecchi et al. 2009).

How do these different formation models compare with the observations reported here? We consider the inclination distribution of binaries with $a/r_H < 0.05$, because these tighter binaries are less susceptible to the KCTF effects discussed above, and should thus represent a better constraint on the formation models. As we discussed above, the binaries with $a/r_H < 0.05$ are predominantly prograde and show a wide range of inclinations up to (and beyond) 90°. This can be compared with the predictions of different formation models. The L^2s model should produce predominantly retrograde orbits (binary inclinations i ~180°), because the L^2s capture occurs in the shear-dominated regime and is essentially two dimensional (e.g., Schlichting & Sari 2008). As for the L^3 model, Schlichting & Sari (2008) quote a slight preference for retrograde orbits (65% retrograde and 35% prograde), because the retrograde orbits are stable to wider separations than the prograde ones. Thus, both the L^2s and L^3 model predictions appear to be contradicted by the observational data.

What are the expectations for the gravitational collapse model? Recent hydrodynamic simulation of the streaming instability (e.g., Simon et al. 2016, 2017) have a sufficiently fine resolution to produce hundreds of gravitationally bound clumps with masses corresponding to diameter 30-300 km planetesimals. Analyzing the properties of the clumps, we find that their rotation is near-critical (i.e., the centrifugal force nearly compensates for the cloud's gravity), just as needed for the efficient formation of binaries. It is also possible to extract from these simulations the orientation of the angular momentum vectors of individual clumps. Since we know from Nesvorný et al. (2010) that the initial angular momentum vectors are a good proxy for the final orientation of binary orbits, we can perform a preliminary comparison with

observations reported here. The results are encouraging, in that most analyzed clumps have prograde rotation and show a wide spread of inclinations. These results may provide additional support for the formation of KBO binaries by the streaming instability, but more work will be needed to analyze the identified trends in more detail.

Acknowledgments

This work is based in part on NASA/ESA Hubble Space Telescope programs 10800, 11113, 11178, 12237, 13404, and 13692. Support for these programs was provided by the National Aeronautics and Space Administration (NASA) through grants from the Space Telescope Science Institute (STScI), operated by the Association of Universities for Research in Astronomy, Inc., (AURA) under NASA contract NAS 5-26555. Further support was provided by Planetary Astronomy Grant AST-1109872 from the National Science Foundation (NSF).

Additional data were obtained at the W.M. Keck Observatory, which is operated as a scientific partnership among the California Institute of Technology, the University of California, and NASA and made possible by the generous financial support of the W.M. Keck Foundation. These data were obtained from telescope time allocated to NASA through the agency's scientific partnership with the California Institute of Technology and the University of California. Acquisition of the data was supported by NASA Keck PI Data Awards, administered by the NASA Exoplanet Science Institute.

Additional data were obtained at the Gemini Observatory, operated by the Association of Universities for Research in Astronomy, Inc., under a cooperative agreement with the NSF on behalf of the Gemini partnership: the National Science Foundation (United States), the National Research Council (Canada), CONICYT (Chile), the Australian Research Council (Australia), Ministério da Ciência, Tecnologia e Inovação (Brazil) and Ministerio de Ciencia, Tecnología e Innovación Productiva (Argentina). The Gemini time was granted through survey program number 2011A-0017 of the National Optical Astronomy Observatory (NOAO). NOAO is managed by AURA under a cooperative agreement with the NSF.

The authors wish to recognize and acknowledge the significant cultural role and reverence of the summit of Mauna Kea within the indigenous Hawaiian community. We are most fortunate to have the opportunity to conduct observations from this mountain.

We wish to express our gratitude to Wm. Robert Johnston for his well-maintained and

comprehensive archive of solar system bodies with satellites (http://www.johnstonsarchive.net/astro/asteroidmoons.html). Thanks also to D. Ragozzine and an anonymous reviewer for constructive feedback on the manuscript and to B. Sands and K. Miller for help with ǀXam names and orthography. Finally, we thank the free and open source software communities for empowering us with key tools used to complete this project, notably Linux, the GNU tools, LibreOffice, MariaDB, Evolution, Python, the Astronomy Users Library, and FVWM.

References

Astakhov, S.A., E.A. Lee, and D. Farrelly 2005. Formation of Kuiper-belt binaries through multiple chaotic scattering encounters with low-mass intruders. *Mon. Not. R. Astron. Soc.* **360,** 401-415.

Bellini, A., J. Anderson, and L.R. Bedin 2011. Astrometry and photometry with HST WFC3 II: Improved geometric-distortion corrections for 10 filters of the UVIS channel. *Publ. Astron. Soc. Pacific* **123,** 622-637.

Benecchi, S.D., K.S. Noll, W.M. Grundy, M.W. Buie, D.C. Stephens, and H.F. Levison 2009. The correlated colors of transneptunian binaries. *Icarus* **200,** 292-303.

Brown, M.E. and T.A. Suer 2007. Satellites of 2003 AZ_84, (50000), (55637), and (90482). *IAU Circ.* No. 8812 #1 .

Brown, M.E. 2013a. On the shape, size, and density of the dwarf planet Makemake. *Astrophys. J. Lett.* **767,** L7.1-5.

Brown, M.E. 2013b. The density of mid-sized Kuiper belt object 2002 UX_{25} and the formation of the dwarf planets. *Astrophys. J. Lett.* **778,** L34.1-5.

Brown, M.E., and B.J. Butler 2017. The density of mid-sized Kuiper belt objects from ALMA thermal observations. *Astron. J.* **154,** 19.1-7.

Brown, M.E., and E.L. Schaller 2007. The mass of dwarf planet Eris. *Science* **316,** 1585-1585.

Brown, M.E., D. Ragozzine, J. Stansberry, and W.C. Fraser 2010. The size, density, and formation of the Orcus-Vanth system in the Kuiper belt. *Astron. J.* **139,** 2700-2705.

Brunini, A. 2019. Flipping the orbital planes of primordial transneptunian binaries by close encounters with Neptune during the planetary instability migration phase of the outer solar system. *Mon. Not. R. Astron. Soc.* **483,** 5042-5044.

Buie, M.W., S.D. Kern, R.L. Millis, L.H. Wasserman, J.L. Elliot, J.A. Pate, J.J. Qu, and B.G.

Marsden 2000. 2000 OH_{67}, 2000 OJ_{67}, 2000 OK_{67}, 2000 OL_{67}, 2000 OM_{67}, 2000 ON_{67}. *Minor Planet Electronic Circ.* 2000-T41.

Buie, M.W., L.H. Wasserman, R.L. Millis, A.A.S. Gulbis, S.D. Kern, D.E. Trilling, J.L. Elliot, and B.G. Marsden 2005. Twenty TNOs and other distant objects. *Minor Planet Electronic Circ.* 2005-G51.

Carry, B., D. Hestroffer, F.E. DeMeo, A. Thirouin, J. Berthier, P. Lacerda, B. Sicardy, A. Doressoundiram, C. Dumas, D. Farrelly, and T.G. Müller 2011. Integral-field spectroscopy of (90482) Orcus-Vanth. *Astron. & Astrophys.* **534,** A115.1-9.

Dolphin, A.E. 2009. A revised characterization of the WFPC2 CTE loss. *Publ. Astron. Soc. Pacific* **121,** 655-667.

Elliot, J.L., et al. (10 co-authors) 2005. The Deep Ecliptic Survey: A search for Kuiper belt objects and Centaurs. II. Dynamical classification, the Kuiper belt plane, and the core population. *Astron. J.* **129,** 1117-1162 (see http://www.boulder.swri.edu/~buie/kbo/desclass.html for current Deep Ecliptic Survey team classifications).

Fang, J., and J.L. Margot 2012. The role of Kozai cycles in near-Earth binary asteroids. *Astron. J.* **143,** 59.1-8.

Fornasier, S., et al. (19 co-authors) 2013. TNOs are Cool: A survey of the transneptunian region VIII. Combined Herschel PACS and SPIRE observations of nine bright targets at 70-500 μm. *Astron. & Astrophys.* **555,** A15.1-22.

Funato, Y., J. Makino, P. Hut, E. Kokubo, and D. Kinoshita 2004. The formation of Kuiper-belt binaries through exchange reactions. *Nature* **427,** 518-520.

Gladman, B., B.G. Marsden, and C. VanLaerhoven 2008. Nomenclature in the outer Solar System. In: A. Barucci, H. Boehnhardt, D. Cruikshank, A. Morbidelli (Eds.), *The Solar System Beyond Neptune*, University of Arizona Press, Tucson, 43-57.

Goldreich, P., Y. Lithwick, and R. Sari 2002. Formation of Kuiper-belt binaries by dynamical friction and three-body encounters. *Nature* **420,** 643-646.

Grundy, W.M., K.S. Noll, J. Virtanen, K. Muinonen, S.D. Kern, D.C. Stephens, J.A. Stansberry, H.F. Levison, and J.R. Spencer 2008. (42355) Typhon-Echidna: Scheduling observations for binary orbit determination. *Icarus* **197,** 260-268.

Grundy, W.M., K.S. Noll, M.W. Buie, S.D. Benecchi, D.C. Stephens, and H.F. Levison 2009. Mutual orbits and masses of six transneptunian binaries. *Icarus* **200,** 627-635.

Grundy, W.M., K.S. Noll, F. Nimmo, H.G. Roe, M.W. Buie, S.B. Porter, S.D. Benecchi, D.C. Stephens, H.F. Levison, and J.A. Stansberry 2011. Five new and three improved mutual orbits of transneptunian binaries. *Icarus* **213,** 678-692.

Grundy, W.M., et al. (11 co-authors) 2012. Mutual events in the cold classical transneptunian binary system Sila and Nunam. *Icarus* **220,** 74-83.

Grundy, W.M., S.D. Benecchi, S.B. Porter, and K.S. Noll 2014. The orbit of transneptunian binary Manwë and Thorondor and their upcoming mutual events. *Icarus* **237,** 1-8.

Grundy, W.M., S.B. Porter, S.D. Benecchi, H.G. Roe, K.S. Noll, C.A. Trujillo, A. Thirouin, J.A. Stansberry, E. Barker, and H.F. Levison 2015. The mutual orbit, mass, and density of the large transneptunian binary system Varda and Ilmarë. *Icarus* **257,** 130-138.

Herriot, G., et al. (21 co-authors) 2000. Progress on Altair: The Gemini North adaptive optics system. *Proc. SPIE* **4007,** 115-125.

Hodapp, K.W., et al. (13 co-authors) 2003. The Gemini Near-Infrared Imager (NIRI). *Publ. Astron. Soc. Pacific* **115,** 1388-1406.

Kavelaars, J.J., B. Gladman, M. Holman, J.M. Petit, H. Scholl, P.D. Nicholson, J.A. Burns B.G. Marsden 1999. 1999 OH_4, 1999 OJ_4, 1999 OK_4, 1999 OL_4, 1999 OM_4, 1999 ON_4, 1999 OO_4. *Minor Planet Electronic Circ.* 1999-W12.

Kominami, J.D., J. Makino, and H. Daisaka 2011. Binary formation in planetesimal disks. I. Equal mass planetesimals. *Publ. Astron. Soc. Japan* **63,** 1331-1344.

Kominami, J.D., and J. Makino 2014. Binary formation in planetesimal disks. II. Planetesimals with a mass spectrum. *Publ. Astron. Soc. Japan* **66,** 123.1-13.

Kozai, Y. 1962. Secular perturbations of asteroids with high inclination and eccentricity. *Astron. J.* **67,** 591-598.

Krist, J.E., R.N. Hook, and F. Stoehr 2011. 20 years of Hubble Space Telescope optical modeling using Tiny Tim. *Proc. SPIE* **8127,** 1-16.

Lee, E.A., S.A. Astakhov, and D. Farrelly 2007. Production of transneptunian binaries through chaos-assisted capture. *Mon. Not. R. Astron. Soc.* **379,** 229-246.

Le Mignant, D., et al. (18 co-authors) 2006. LGS AO at W.M. Keck Observatory: Routine operations and remaining challenges. *Proc. SPIE* **6272,** 627201.

Lidov, M.L. 1962. The evolution of orbits of artificial satellites of planets under the action of gravitational perturbations of external bodies. *Planet. Space. Sci.* **9,** 719-759.

Jewitt, D., and J. Luu 1993. Discovery of the candidate Kuiper belt object 1992 QB_1. *Nature* **362,** 730-732.

Jewitt, D.C., S.S. Sheppard, J. Kleyna, and B.G. Marsden 2002. 2001 XP_{254}, 2001 XQ_{254}, 2001 XR_{254}. *Minor Planet Electronic Circ.* 2002-A70.

Marchis, F., M. Baek, J. Berthier, P. Descamps, F. Vachier, K.S. Noll, S.D. Kern, and W.M. Grundy 2008. (119067) 2001 KP_76 and (160091) 2000 OL_67. *IAU Circ.* No. 8922 #2.

McMaster, M., et al. (39 co-authors) 2008. *WFPC2 instrument handbook*, Version 10.0. Space Telescope Science Institute, Baltimore, available at http://www.stsci.edu/hst/wfpc2.

Millis, R.L., et al. (10 co-authors) 1999. 1998 WW_{31}. *Minor Planet Electronic Circ.* 1999-B24.

Millis, R.L., M.W. Buie, R.M. Wagner, J.L. Elliot, P. Smith, J. Christensen, D. Wilmarth, J.W. Parker, L.H. Wasserman, and B.G. Marsden 2000. 2000 CM_{114}, 2000 CN_{114}, 2000 CO_{114}, 2000 CP_{114}, 2000 CQ_{114}. *Minor Planet Electronic Circ.* 2000-J45.

Naoz, S., H.B. Perets, and D. Ragozzine 2010. The observed orbital properties of binary minor planets. *Astrophys. J.* **719,** 1775-1783.

Nazzario, R.C., K. Orr, C. Covington, D. Kagan, and T.W. Hyde 2007. Kuiper binary formation. *Adv. Space Res.* **40,** 280-283.

Nelder, J., and R. Mead 1965. A simplex method for function minimization. *Computer Journal* **7,** 308-313.

Nesvorný, D., A.N. Youdin, and D.C. Richardson 2010. Formation of Kuiper belt binaries by gravitational collapse. *Astron. J.* **140,** 785-793.

Nesvorný, D., D. Vokrouhlický, W.F. Bottke, K. Noll, and H.F. Levison 2011. Observed binary fraction sets limits on the extent of collisional grinding in the Kuiper belt. *Astron. J.* **141,** 159.1-11.

Nicholson, P.D., M. Cuk, S.S. Sheppard, D. Nesvorný, and T.V. Johnson 2008. Irregular satellites of the giant planets. In: A. Barucci, H. Boehnhardt, D. Cruikshank, A. Morbidelli (Eds.), *The Solar System Beyond Neptune*, University of Arizona Press, Tucson, 411-424.

Noll, K.S., W.M. Grundy, H.F. Levison, and D.C. Stephens 2006a. (60458) 2000 CM_114. *IAU Circ.* No. 8689 #2.

Noll, K.S., D.C. Stephens, W.M. Grundy, and H.F. Levison 2006b. 2000 QL_251. *IAU Circ.* No. 8746 #1.

Noll, K.S., H.F. Levison, D.C. Stephens, and W.M. Grundy 2006c. (120347) 2004 SB_60. *IAU*

Circ. No. 8751 #1.

Noll, K.S., W.M. Grundy, H.F. Levison, and D.C. Stephens 2006d. 1999 RT_214. *IAU Circ.* No. 8756 #2.

Noll, K.S., W.M. Grundy, S.D. Kern, H.F. Levison, and D.C. Stephens 2007a. (119979) 2002 WC_19. *IAU Circ.* No. 8814 #1.

Noll, K.S., S.D. Kern, W.M. Grundy, D.C. Stephens, and H.F. Levison 2007b. (160256) 2002 PD_149. *IAU Circ.* No. 8866 #3.

Noll, K.S., W.M. Grundy, E.I. Chiang, J.L. Margot, and S.D. Kern 2008. Binaries in the Kuiper belt. In: A. Barucci, H. Boehnhardt, D. Cruikshank, A. Morbidelli (Eds.), *The Solar System Beyond Neptune*, University of Arizona Press, Tucson, 345-363.

Noll, K.S., W.M. Grundy, S.D. Benecchi, H.F. Levison, and E.A. Barker 2009. Discovery of eighteen transneptunian binaries. *Bull. Amer. Astron. Soc.* **41,** 1092 (abstract).

Parker, A.H., J.J. Kavelaars, J.M. Petit, L. Jones, B. Gladman, and J. Parker 2011. Characterization of seven ultra-wide transneptunian binaries. *Astrophys. J.* **743,** 1.1-20.

Perets, H.B., and S. Naoz 2009. Kozai cycles, tidal friction, and the dynamical evolution of binary minor planets. *Astrophys. J.* **699,** L17-L21.

Petit, J.M., and O. Mousis 2004. KBO binaries: How numerous are they? *Icarus* **168,** 409-419.

Petit, J.M., et al. (16 co-authors) 2011. The Canada-France Ecliptic Plane Survey - full data release: The orbital structure of the Kuiper belt. *Astron. J.* **142,** 131.1-24.

Porter, S.B., and W.M. Grundy 2012. KCTF evolution of transneptunian binaries: Connecting formation to observation. *Icarus* **220,** 947-957.

Press, W.H., S.A. Teukolsky, W.T. Vetterling, and B.P. Flannery 1992. *Numerical Recipes in C*. Cambridge University Press, New York.

Roe, H.G., M.E. Brown, K.M. Barkume, and B.G. Marsden 2005. 2004 SB_{60}, 2004 SC_{60}, 2005 EW_{318}, 2005 EX_{318}, 2005 GX_{206}, 2005 GY_{206}, 2005 GZ_{206}. *Minor Planet Electronic Circ.* 2005-J26.

Schlichting, H.E., and R. Sari 2008. The ratio of retrograde to prograde orbits: A test for Kuiper belt binary formation theories. *Astrophys. J.* **686,** 741-747.

Schultz, A.B., et al. (15 co-authors) 2003. Post-NCS performance of the HST NICMOS. *Proc. SPIE* **4850,** 858-866.

Shannon, A., Y. Wu, and Y. Lithwick 2016. Forming the cold classical Kuiper belt in a light disk.

Astrophys. J. **818,** 175.1-11.

Sheppard, S.S., D. Ragozzine, and C. Trujillo 2012. 2007 TY_{430}: A cold classical Kuiper belt type binary in the Plutino population. *Astron. J.* **143,** 58.1-13.

Simon, J.B., P.J. Armitage, R. Li, and A.N. Youdin 2016. The mass and size distribution of planetesimals formed by the streaming instability. I: The role of self-gravity. *Astrophys. J.* **822,** 55.1-18.

Simon, J.B., P.J. Armitage, A.N. Youdin, and R. Li 2017. Evidence for universality in the initial planetesimal mass function. *Astrophys. J. Lett.* **847,** L12.1-6.

Sirianni, M., et al. (13 co-authors) 2005. The photometric performance and calibration of the Hubble Space Telescope Advanced Camera for Surveys. *Publ. Astron. Soc. Pacific* **117,** 1049-1112.

Skinner, C.J., and 17 co-authors 1998. On-orbit properties of the NICMOS detectors on HST. *Proc. SPIE* **3354,** 2-13.

Stansberry, J.A., W.M. Grundy, M. Mueller, S.D. Benecchi, G.H. Rieke, K.S. Noll, M.W. Buie, H.F. Levison, S.B. Porter, and H.G. Roe 2012. Physical properties of transneptunian binaries (120347) Salacia-Actaea and (42355) Typhon-Echidna. *Icarus* **219,** 676-688.

Stephens, D.C., K.S. Noll, and W.M. Grundy 2004. 2000 CQ_114. *IAU Circ.* No. 8289, #1.

Stephens, D.C., and K.S. Noll 2006. Detection of six trans-neptunian binaries with NICMOS: A high fraction of binaries in the cold classical disk. *Astron. J.* **131,** 1142-1148.

Trujillo, C.A., J.X. Luu, D.C. Jewitt, S. Sheppard, and B.G. Marsden 1999. 1999 RT_{214}. *Minor Planet Electronic Circ.* 1999-X27.

Trujillo, C.A., M.E. Brown, E.F. Helin, S. Pravdo, K. Lawrence, M. Hicks, and B.G. Marsden 2003. 2002 WC_{19}, 2002 XV_{93}, 2002 XW_{93}. *Minor Planet Electronic Circ.* 2003-A25.

Veillet, C., J.W. Parker, I. Griffin, B. Marsden, A. Doressoundiram, M. Buie, D.J. Tholen, M. Connelley, and M.J. Holman 2002. The binary Kuiper-belt object 1998 WW_{31}. *Nature* **416,** 711-713.

Vilenius, E., et al. (22 co-authors) 2012. "TNOs are Cool": A survey of the trans-neptunian region. VI. Herschel/PACS observations and thermal modeling of 19 classical Kuiper belt objects. *Astron. & Astrophys.* **541,** A94.1-17.

Vilenius, E., et al. (16 co-authors) 2014. "TNOs are Cool": A survey of the trans-neptunian region X. Analysis of classical Kuiper belt objects from Herschel and Spitzer observations.

Astron. & Astrophys. **564,** A35.1-18.

Wasserman, L.H., M.W. Buie, S.D. Kern, R.L. Millis, J.L. Elliot, and B.G. Marsden 2001. Seven TNOs. *Minor Planet Electronic Circ.* 2001-M34.

Wasserman, L.H., D.E. Trilling, R.L. Millis, M.W. Buie, S.D. Kern, E.I. Chiang, K.B. Clancy, and B.G. Marsden 2003. 2002 XD_{91}, 2002 XE_{91}, 2002 XF_{91}, 2002 XG_{91}, 2002 XH_{91}, 2002 XJ_{91}. *Minor Planet Electronic Circ.* 2003-A05.

Wasserman, L.H., and 16 co-authors 2004. 2003 KO_{20}, 2003 QA_{91}, 2003 QB_{92}. *Minor Planet Electronic Circ.* 2004-R12.

Weidenschilling, S.J. 2002. On the origin of binary transneptunian objects. *Icarus* **160,** 212-215.

Youdin, A.N., and J. Goodman 2005. Streaming instabilities in protoplanetary disks. *Astrophys. J.* **620,** 459-469.

Table 1

Observation circumstances and relative astrometry for transneptunian binaries

UT date and time		Telescope/ instrument	*r* (AU)	Δ (AU)	*g* (deg.)	Δ*x* (arcsec)	Δ*y* (arcsec)
60458 2000 CM_{114}							
2006-01-19	$6^h.8165$	HST/ACS HRC	42.155	41.239	0.49	0.03376(39)	−0.07140(78)
2007-10-25	$17^h.8186$	HST/WFPC2	41.590	41.949	1.27	0.0293(33)	−0.0761(33)
2007-12-06	$5^h.1186$	HST/WFPC2	41.554	41.212	1.28	−0.0540(22)	0.0300(53)
2008-01-18	$9^h.5408$	HST/WFPC2	41.517	40.630	0.60	0.0141(21)	0.0818(49)
2015-03-10	$8^h.1017$	HST/WFC3 UVIS	39.419	38.473	0.44	0.0018(10)	0.0858(12)
2015-04-02	$15^h.6723$	HST/WFC3 UVIS	39.402	38.636	0.94	0.0275(22)	0.0787(22)
90482 Orcus and Vanth							
2005-11-13	$3^h.7241$	HST/ACS HRC	47.705	47.811	1.18	0.2079(49)	−0.1434(99)
2006-10-31	$20^h.8712$	HST/ACS HRC	47.752	48.075	1.12	0.2260(10)	−0.11307(71)
2006-11-03	$1^h.6039$	HST/ACS HRC	47.753	48.041	1.14	−0.09310(50)	−0.22635(50)
2006-11-04	$20^h.7813$	HST/ACS HRC	47.753	48.013	1.14	−0.25893(50)	−0.00560(79)
2006-11-12	$1^h.8969$	HST/ACS HRC	47.754	47.898	1.17	−0.0069(19)	−0.24344(50)
2006-11-16	$14^h.1272$	HST/ACS HRC	47.754	47.824	1.18	−0.03718(58)	0.24113(50)
2006-11-26	$15^h.5108$	HST/ACS HRC	47.756	47.660	1.18	0.05228(85)	0.24033(50)
2006-12-10	$20^h.0630$	HST/ACS HRC	47.757	47.433	1.12	−0.03180(50)	−0.24410(50)
2007-11-11	$19^h.0320$	HST/NICMOS	47.799	47.968	1.17	−0.2630(50)	−0.0240(50)
2007-12-05	$6^h.7256$	HST/WFPC2	47.802	47.585	1.16	0.2429(24)	0.0781(42)
2010-02-23	$5^h.6846$	VLT/SINFONI	47.890	46.954	0.39	0.260(25)	0.052(25)
2015-04-05	$9^h.1200$	Keck/NIRC2	48.036	47.307	0.82	−0.0785(10)	0.2297(10)
119979 2002 WC_{19}							
2006/11/05	$23^h.4002$	HST/ACS HRC	43.218	42.351	0.64	−0.08206(98)	−0.0662(11)
2007/08/06	$19^h.3489$	HST/WFPC2	43.035	43.526	1.17	+0.072(15)	+0.0395(55)
2007/08/25	$20^h.5350$	HST/WFPC2	43.022	43.213	1.32	−0.1135(21)	−0.0565(38)
2009/09/30	$21^h.4364$	HST/WFC3 UVIS	42.514	42.143	1.26	−0.0116(75)	−0.057(17)
2009/12/12	$8^h.3271$	Keck/NIRC2	42.466	41.489	0.17	−0.08950(53)	−0.0220(23)
2013/10/12	$0^h.5369$	HST/WFC3 UVIS	41.553	41.096	1.23	+0.1058(47)	+0.0156(43)
2014/01/03	$14^h.2940$	HST/WFC3 UVIS	41.499	40.591	0.53	+0.0820(59)	+0.032(12)
120347 Salacia and Actaea							

2006/07/21	$21^h.9583$	HST/ACS HRC	43.789	43.164	1.06	+0.04706(70)	−0.10224(50)
2007/07/13	$21^h.1017$	HST/WFPC2	43.880	43.375	1.16	+0.0219(39)	−0.111(13)
2007/07/15	$19^h.9142$	HST/WFPC2	43.880	43.350	1.14	+0.1237(45)	+0.0921(21)
2007/08/11	$11^h.1392$	HST/WFPC2	43.887	43.077	0.80	+0.1778(20)	+0.0036(30)
2007/08/12	$6^h.6864$	HST/WFPC2	43.887	43.071	0.79	+0.1279(39)	+0.0940(19)
2007/08/12	$9^h.8156$	HST/WFPC2	43.887	43.070	0.79	+0.1008(86)	+0.0989(32)
2007/09/03	$9^h.7183$	HST/WFPC2	43.893	42.970	0.54	+0.1031(36)	+0.0995(35)
2008/05/19	$18^h.5686$	HST/WFPC2	43.958	44.288	1.24	−0.1010(20)	+0.0742(20)
2009/12/11	$6^h.5120$	Keck 2/NIRC2	44.098	44.081	1.28	+0.0580(61)	+0.1056(30)
2010/08/03	$9^h.7339$	Keck 2/NIRC2	44.155	43.455	0.96	+0.1827(30)	+0.0184(30)
2013/07/18	$12^h.6403$	Gemini N/NIRI	44.402	43.941	1.17	−0.20(10)	−0.08(10)
2013/08/24	$12^h.2928$	Gemini N/NIRI	44.410	43.568	0.73	−0.07(10)	+0.12(10)
2015/07/31	$11^h.8537$	Keck 2/NIRC2	44.565	43.980	1.07	+0.0587(31)	−0.0822(65)
2016/08/06	$11^h.2366$	Keck 2/NIRC2	44.646	43.999	1.01	−0.1806(30)	−0.0519(30)
160091 2000 OL_{67}							
2007/06/26	$10^h.8572$	HST/WFPC2	42.887	42.559	1.29	+0.246(10)	+0.0367(20)
2009/12/12	$5^h.7406$	Keck 2/NIRC2	43.132	43.179	1.31	−0.1634(30)	+0.0301(30)
2012/08/07	$13^h.0111$	Gemini N/NIRI	43.393	42.580	0.81	−0.06(10)	−0.29(10)
2012/08/13	$12^h.2547$	Gemini N/NIRI	43.395	42.526	0.69	−0.01(10)	−0.09(10)
2013/10/24	$8^h.0768$	Keck 2/NIRC2	43.512	42.731	0.82	−0.1181(69)	+0.1502(69)
2015/09/05	$8^h.8367$	Keck 2/NIRC2	43.698	42.717	0.31	−0.1711(48)	+0.0953(56)
2017/08/25	$9^h.9681$	Keck 2/NIRC2	43.900	42.992	0.58	−0.0711(95)	+0.1929(46)
160256 2002 PD_{149}							
2007/05/22	$4^h.8739$	HST/WFPC2	45.213	45.593	1.18	+0.6601(24)	+0.3632(11)
2009/12/12	$6^h.9216$	Keck 2/NIRC2	45.137	45.064	1.25	+1.0598(30)	+0.0593(62)
2012/08/24	$13^h.1569$	Gemini N/NIRI	45.043	44.145	0.60	−0.194(50)	+0.024(50)
2014/08/19	$12^h.5963$	Keck 2/NIRC2	44.966	44.137	0.75	+1.0360(18)	+0.0679(49)
2015/09/05	$10^h.2321$	Keck 2/NIRC2	44.925	43.979	0.45	+1.1782(50)	+0.3377(50)
469514 2003 QA_{91}							
2006/06/19	$8^h.8562$	HST/ACS HRC	45.062	44.580	1.14	−0.0165(16)	+0.0469(14)
2009/09/15	$16^h.5885$	HST/WFC3 UVIS	44.864	43.921	0.45	+0.0475(17)	−0.0128(24)
2009/09/16	$0^h.9557$	HST/WFC3 UVIS	44.864	43.923	0.46	+0.0470(30)	−0.0046(44)
2009/09/17	$3^h.3179$	HST/WFC3 UVIS	44.864	43.930	0.48	−0.0397(17)	−0.0292(24)

2010/04/15	$0^h.4671$	HST/WFC3 UVIS	44.827	45.461	0.99	+0.0320(34)	−0.0360(30)
2010/04/19	$1^h.9379$	HST/WFC3 UVIS	44.827	45.406	1.04	+0.0124(31)	−0.0472(29)
2014/08/19	$10^h.8596$	Keck 2/NIRC2	44.541	43.554	0.29	−0.0393(30)	+0.0264(30)
2015/09/05	$9^h.8275$	Keck 2/NIRC2	44.473	43.466	0.07	+0.0206(30)	+0.0441(30)
2016/08/06	$11^h.7155$	Keck 2/NIRC2	44.413	43.512	0.60	−0.0389(30)	+0.0303(30)
2017/08/25	$8^h.9776$	Keck 2/NIRC2	44.347	43.353	0.24	−0.0433(30)	+0.0205(30)
2017/08/26	$9^h.8115$	Keck 2/NIRC2	44.347	43.350	0.22	−0.0492(45)	−0.0061(30)
469705 ǂKágára and !Hãunu							
2009/01/21	$11^h.6061$	HST/WFPC2	40.819	40.005	0.78	+0.0979(16)	−0.0579(12)
2011/03/20	$2^h.4324$	HST/WFC3 UVIS	40.705	39.776	0.51	+0.0412(40)	−0.0523(23)
2011/03/27	$19^h.6747$	HST/WFC3 UVIS	40.704	39.829	0.68	+0.003(20)	+0.016(20)
2011/04/18	$7^h.2403$	Gemini N/NIRI	40.699	40.053	1.09	−0.170(50)	+0.050(50)
2011/04/22	$12^h.1457$	HST/WFC3 UVIS	40.701	40.110	1.15	−0.1476(21)	+0.0544(10)
2011/05/10	$17^h.3792$	HST/WFC3 UVIS	40.698	40.382	1.36	−0.2242(41)	+0.0920(22)
2011/07/08	$20^h.5321$	HST/WFC3 UVIS	40.690	41.316	1.12	+0.1016(42)	−0.0625(37)
2012/02/03	$14^h.7431$	Gemini N/NIRI	40.662	39.775	0.61	−0.2391(30)	+0.117(10)
2012/03/18	$11^h.4842$	HST/WFC3 UVIS	40.656	39.713	0.45	+0.0908(22)	−0.0535(14)
2013/03/21	$11^h.3223$	Keck 2/NIRC2	40.607	39.671	0.49	−0.1803(45)	+0.1132(34)
508788 2000 CQ_{114}							
2003/06/06	$0^h.5650$	HST/NICMOS	45.434	45.540	1.27	−0.1782(34)	−0.041(16)
2007/11/11	$13^h.3186$	HST/WFPC2	45.913	46.355	1.10	+0.1723(18)	+0.0842(28)
2007/12/02	$21^h.7769$	HST/WFPC2	45.919	46.007	1.22	+0.2162(24)	+0.0564(11)
2008/01/06	$3^h.8144$	HST/WFPC2	45.929	45.442	1.07	+0.1588(18)	−0.0206(17)
2008/03/23	$8^h.8887$	HST/WFPC2	45.952	45.005	0.39	−0.1855(16)	−0.0635(22)
2014/04/01	$1^h.5833$	HST/WFC3 UVIS	46.595	45.653	0.41	−0.1691(25)	−0.0710(27)
2015/04/04	$4^h.7068$	HST/WFC3 UVIS	46.701	45.769	0.45	+0.1762(15)	−0.0260(37)
508869 2002 VT_{130}							
2008/09/21	$22^h.3075$	HST/WFPC2	42.823	42.462	1.26	+0.0428(19)	−0.0688(15)
2009/12/12	$9^h.2874$	Keck 2/NIRC2	42.858	41.893	0.27	−0.0519(21)	+0.0586(10)
2012/10/28	$10^h.5510$	Gemini N/NIRI	42.937	42.153	0.82	−0.0861(39)	−0.0291(30)
2013/08/23	$14^h.2824$	Gemini N/NIRI	42.960	43.204	1.31	−0.0006(30)	+0.0886(30)
2013/10/24	$9^h.4242$	Keck 2/NIRC2	42.965	42.243	0.92	+0.0003(16)	+0.0912(13)
2013/10/25	$9^h.9504$	Keck 2/NIRC2	42.965	42.231	0.90	−0.0176(10)	+0.0821(10)

1998 WW_{31}							
2001/07/12	$21^h.5835$	HST/WFPC2	46.763	47.358	1.00	+0.4808(24)	+0.7393(32)
2001/08/09	$18^h.9614$	HST/WFPC2	46.769	46.933	1.22	+0.3725(54)	+0.6702(71)
2001/09/10	$16^h.4014$	HST/WFPC2	46.775	46.408	1.15	+0.2121(58)	+0.5479(29)
2001/12/30	$11^h.6838$	HST/WFPC2	46.795	46.074	0.83	+0.4128(57)	+0.0595(25)
2002/01/19	$12^h.5671$	HST/WFPC2	46.799	46.357	1.08	+0.5404(47)	+0.1579(51)
2002/02/24	$5^h.5281$	HST/WFPC2	46.805	46.968	1.19	+0.6953(74)	+0.3200(39)
2002/07/13	$2^h.1190$	HST/WFPC2	46.831	47.442	0.99	+0.9049(61)	+0.7330(68)
2002/08/14	$1^h.6690$	HST/WFPC2	46.837	46.953	1.23	+0.9013(37)	+0.7931(51)
2002/09/13	$17^h.2395$	HST/WFPC2	46.842	46.449	1.14	+0.8949(37)	+0.8360(50)
2002/10/14	$11^h.8026$	HST/WFPC2	46.848	46.048	0.74	+0.8598(43)	+0.8652(20)
2002/11/13	$1^h.4742$	HST/WFPC2	46.853	45.871	0.15	+0.8055(37)	+0.8720(32)
2002/12/13	$16^h.6394$	HST/WFPC2	46.859	45.962	0.50	+0.7220(37)	+0.8635(20)
2003/01/14	$20^h.3510$	HST/WFPC2	46.865	46.332	1.02	+0.6134(53)	+0.8286(56)
2003/02/13	$9^h.8693$	HST/WFPC2	46.870	46.823	1.21	+0.5120(43)	+0.7656(23)
2012/11/03	$12^h.5142$	Gemini N/NIRI	47.472	46.589	0.55	+0.499(50)	+0.625(50)
2013/10/25	$9^h.6302$	Keck 2/NIRC2	47.527	46.739	0.74	+0.9431(36)	+0.6864(17)
1999 OJ_4							
2002/10/04	$14^h.3591$	HST/NICMOS	38.165	37.550	1.19	−0.0353(42)	+0.071(10)
2005/07/24	$16^h.9878$	HST/ACS HRC	38.087	37.149	0.59	+0.09392(56)	+0.03652(57)
2007/07/05	$23^h.3058$	HST/WFPC2	38.033	37.303	1.08	−0.0152(22)	−0.1444(13)
2007/07/07	$10^h.5933$	HST/WFPC2	38.033	37.286	1.05	−0.0209(17)	−0.1448(10)
2007/07/12	$21^h.1017$	HST/WFPC2	38.033	37.226	0.94	−0.0515(28)	−0.1356(10)
2007/08/01	$22^h.2017$	HST/WFPC2	38.031	37.067	0.48	−0.0735(23)	+0.0034(45)
2007/08/24	$9^h.4206$	HST/WFPC2	38.030	37.021	0.10	+0.1070(25)	+0.0093(14)
2012/08/06	$12^h.0153$	Gemini N/NIRI	37.895	36.948	0.55	−0.043(50)	−0.090(50)
2013/10/25	$5^h.5169$	Keck 2/NIRC2	37.862	37.302	1.25	−0.0373(10)	+0.0505(10)
2015/09/05	$11^h.9608$	Keck 2/NIRC2	37.813	36.807	0.10	+0.0472(26)	+0.0772(31)
1999 RT_{214}							
2006/07/25	$6^h.2623$	HST/ACS HRC	40.638	39.727	0.64	+0.11331(84)	+0.00059(30)
2008/05/29	$13^h.4313$	HST/WFPC2	40.610	40.486	1.42	−0.0703(38)	+0.0150(61)
2008/09/07	$9^h.4158$	HST/WFPC2	40.606	39.629	0.35	+0.1010(32)	+0.0269(38)
2014/10/05	$4^h.8898$	HST/WFC3 UVIS	40.544	39.699	0.76	−0.0449(14)	−0.0711(30)

2014/11/04	$1^h.9441$	HST/WFC3 UVIS	40.544	40.080	1.25	+0.0685(37)	−0.0343(25)
2017/08/26	$9^h.3363$	Keck 2/NIRC2	40.531	39.539	0.28	+0.1027(25)	+0.0069(58)
2000 QL_{251}							
2006/07/25	$10^h.7690$	HST/ACS HRC	38.814	38.274	1.28	−0.24089(45)	−0.10082(50)
2007/07/15	$22^h.7517$	HST/WFPC2	38.932	38.566	1.40	−0.1021(29)	−0.1700(12)
2007/07/19	$9^h.8100$	HST/WFPC2	38.933	38.513	1.37	−0.0501(12)	−0.1582(22)
2007/08/05	$11^h.7683$	HST/WFPC2	38.939	38.277	1.14	−0.0223(26)	+0.0814(19)
2007/08/27	$17^h.9405$	HST/WFPC2	38.947	38.053	0.70	−0.2334(19)	−0.1259(18)
2008/08/25	$8^h.6061$	HST/WFPC2	39.073	38.206	0.77	+0.0742(13)	−0.0680(15)
2009/12/19	$12^h.1919$	HST/WFC3 UVIS	39.246	39.132	1.43	−0.2355(20)	−0.1091(32)
2012/09/29	$10^h.0003$	Gemini N/NIRI	39.636	38.637	0.09	−0.244(20)	−0.103(20)
2015/07/31	$14^h.8277$	Keck 2/NIRC2	40.064	39.659	1.34	−0.0392(80)	−0.1513(41)
2017/08/08	$14^h.3100$	Keck 2/NIRC2	40.387	39.901	1.27	+0.0425(45)	−0.1130(56)
2001 XR_{254}							
2006-12-20	6.6769	HST/ACS HRC	44.162	43.232	0.42	0.10693(98)	−0.01285(52)
2007-09-17	11.1853	HST/WFPC2	44.149	44.563	1.18	−0.3043(14)	0.1517(11)
2007-09-18	2.4936	HST/WFPC2	44.149	44.553	1.19	−0.3048(19)	0.1560(10)
2007-09-21	7.6645	HST/WFPC2	44.149	44.502	1.22	−0.3147(16)	0.1654(10)
2007-10-09	2.6269	HST/WFPC2	44.148	44.204	1.29	−0.3050(14)	0.1984(16)
2007-12-05	9.9554	HST/WFPC2	44.145	43.345	0.75	−0.1032(10)	−0.0138(19)
2007-12-28	14.6145	HST/WFPC2	44.144	43.182	0.27	0.018(18)	0.0245(70)
2009-12-12	10.0100	Keck 2/NIRC2	44.111	43.262	0.66	−0.0447(30)	0.1044(30)
2002 XH_{91}							
2008/11/08	$23^h.0342$	HST/WFPC2	47.559	47.068	1.04	+0.5405(31)	+0.2150(23)
2012/04/12	$6^h.4571$	Gemini N/NIRI	47.451	47.504	1.21	−0.206(10)	+0.214(15)
2012/11/06	$14^h.3782$	Gemini N/NIRI	47.432	47.044	1.11	+0.731(11)	+0.121(11)
2015/04/05	$7^h.9303$	Keck 2/NIRC2	47.345	47.211	1.20	−0.0295(38)	+0.3368(15)
2017/12/09	$13^h.5779$	Keck 2/NIRC2	47.240	46.477	0.76	+0.7849(30)	+0.0909(38)
2003 TJ_{58}							
2006/11/22	$5^h.8297$	HST/ACS HRC	40.912	39.966	0.40	+0.1001(12)	+0.06001(92)
2007/08/12	$1^h.6364$	HST/WFPC2	40.939	41.427	1.24	+0.0907(31)	−0.0059(24)
2007/09/03	$2^h.4072$	HST/WFPC2	40.941	41.076	1.40	+0.0864(18)	+0.1006(15)
2007/10/22	$16^h.8825$	HST/WFPC2	40.946	40.294	1.06	−0.0575(14)	+0.1616(23)

2007/11/20	$6^h.2408$	HST/WFPC2	40.949	40.022	0.48	−0.1074(22)	+0.0777(25)
2014/01/10	$13^h.6518$	HST/WFC3 UVIS	41.213	40.316	0.57	+0.1100(38)	+0.0011(33)

Table notes:

[a.] The distance from the Sun to the target is r and from the observer to the target is Δ. The phase angle g is the angular separation between the observer and Sun as seen from the target.

[b.] Relative right ascension Δx and relative declination Δy are computed as $\Delta x = (\alpha_2 - \alpha_1)\cos(\delta_1)$ and $\Delta y = \delta_2 - \delta_1$, where α is right ascension, δ is declination, and subscripts 1 and 2 refer to primary and secondary, respectively. Estimated 1-σ uncertainties in the final 2 digits are indicated in parentheses.

Table 2

Orbit solution and 1-σ uncertainties for 60458 2000 CM_{114} and its satellite

Parameter		Value
Fitted elements[a]		
Period (days)	P	24.8254 ± 0.0013
Semimajor axis (km)	a	2497 ± 25
Eccentricity	e	0.035 ± 0.011
Inclination[b] (deg)	i	76.0 ± 1.6
Mean longitude[b] at epoch[c] (deg)	ϵ	116.0 ± 2.6
Longitude of asc. node[b] (deg)	Ω	284.9 ± 2.1
Longitude of periapsis[b] (deg)	ϖ	115 ± 23
Derived parameters		
Standard gravitational parameter GM_{sys} (km^3 s^{-2})	μ	0.1337 ± 0.0040
System mass (10^{18} kg)	M_{sys}	2.003 ± 0.061
Orbit pole right ascension[b] (deg)	α_{pole}	194.9 ± 2.0
Orbit pole declination[b] (deg)	δ_{pole}	14.0 ± 1.6
Orbit pole ecliptic longitude[d] (deg)	λ_{pole}	188.1 ± 2.0
Orbit pole ecliptic latitude[d] (deg)	β_{pole}	18.8 ± 1.7
Inclination to heliocentric orbit (deg)		55.6 ± 1.9
Next mutual events season (year)		2079

Table notes:

[a.] Elements are for the secondary relative to the primary. The average sky plane residual is 3.3 mas and the maximum is 7.8 mas; χ^2 is 11.1, based on observations at 6 epochs. The mirror orbit solution has a much worse χ^2 = 23.2 allowing us to exclude it with 3.6 σ confidence.

[b.] Referenced to J2000 equatorial frame.

[c.] The epoch is Julian date 2457000, corresponding to 2014 December 8 12:00 UT.

[d.] Referenced to J2000 ecliptic frame.

Table 3

Orbit solution and 1-σ uncertainties for Orcus and its satellite Vanth

Parameter		Value
Fitted elements[a]		
Period (days)	P	9.539154 ± 0.000020
Semimajor axis (km)	a	8999.8 ± 9.1
Eccentricity	e	0.00091 ± 0.00053
Inclination[b] (deg)	i	105.03 ± 0.18
Mean longitude[b] at epoch[c] (deg)	ϵ	188.52 ± 0.39
Longitude of asc. node[b] (deg)	Ω	53.49 ± 0.33
Longitude of periapsis[b] (deg)	ϖ	328 ± 51
Derived parameters		
Standard gravitational parameter GM_{sys} (km^3 s^{-2})	μ	42.37 ± 0.13
System mass (10^{18} kg)	M_{sys}	634.8 ± 1.9
Orbit pole right ascension[b] (deg)	α_{pole}	323.49 ± 0.32
Orbit pole declination[b] (deg)	δ_{pole}	−15.03 ± 0.15
Orbit pole ecliptic longitude[d] (deg)	λ_{pole}	320.92 ± 0.29
Orbit pole ecliptic latitude[d] (deg)	β_{pole}	−0.54 ± 0.17
Inclination to heliocentric orbit (deg)		106.71 ± 0.22
Next mutual events season (year)		2082

Table notes:

[a.] Elements are for Vanth relative to Orcus. The average sky plane residual is 2.6 mas and the maximum is 7.3 mas; χ^2 is 31.8, based on observations at 12 epochs. The mirror orbit solution has a much worse $\chi^2 = 124$, allowing us to confidently exclude it.

[b.] Referenced to J2000 equatorial frame.

[c.] The epoch is Julian date 2454000, corresponding to 2006 September 21 12:00 UT.

[d.] Referenced to J2000 ecliptic frame.

Table 4

Orbit solutions and 1-σ uncertainties for 119979 2002 WC_{19} and its satellite

Parameter		Orbit 1 value	Orbit 2 value
Fitted elements[a]		$\chi^2 = 13.9$	$\chi^2 = 15.4$
Period (days)	P	8.40179 ± 0.00024	8.40366 ± 0.00026
Semimajor axis (km)	a	4169 ± 17	4015 ± 16
Eccentricity	e	0.222 ± 0.026	0.189 ± 0.038
Inclination[b] (deg)	i	23.97 ± 0.72	141.31 ± 0.58
Mean longitude[b] at epoch[c] (deg)	ϵ	261.1 ± 2.0	319.7 ± 2.7
Longitude of asc. node[b] (deg)	Ω	67.0 ± 1.4	206.1 ± 1.2
Longitude of periapsis[b] (deg)	ϖ	261.8 ± 1.4	331.0 ± 3.5
Derived parameters			
Standard gravitational parameter GM_{sys} ($km^3\ s^{-2}$)	μ	5.427 ± 0.067	4.848 ± 0.058
System mass (10^{18} kg)	M_{sys}	81.3 ± 1.0	72.63 ± 0.87
Orbit pole right ascension[b] (deg)	α_{pole}	337.0 ± 1.4	116.1 ± 1.0
Orbit pole declination[b] (deg)	δ_{pole}	66.03 ± 0.70	−51.31 ± 0.56
Orbit pole ecliptic longitude[d] (deg)	λ_{pole}	30.2 ± 1.8	143.3 ± 1.8
Orbit pole ecliptic latitude[d] (deg)	β_{pole}	64.34 ± 0.46	−69.96 ± 0.59
Inclination to heliocentric orbit (deg)		16.80 ± 0.48	163.24 ± 0.59
Next mutual events season (year)		2042	2085

Table notes:

[a.] Elements are for secondary relative to primary. The average sky plane residual for Orbit 1 is 9 mas and the maximum is 28 mas. For Orbit 2 the average residual is 12 mas.

[b.] Referenced to J2000 equatorial frame.

[c.] The epoch is Julian date 2457000, corresponding to 2014 December 8 12:00 UTC.

[d.] Referenced to J2000 ecliptic frame.

Table 5

Orbit solution and 1-σ uncertainties for Salacia and its satellite Actaea

Parameter		Value
Fitted elements[a]		
Period (days)	P	5.493882 ± 0.000023
Semimajor axis (km)	a	5724 ± 27
Eccentricity	e	0.0098 ± 0.0038
Inclination[b] (deg)	i	23.59 ± 0.36
Mean longitude[b] at epoch[c] (deg)	ϵ	303.76 ± 0.36
Longitude of asc. node[b] (deg)	Ω	45.2 ± 1.6
Longitude of periapsis[b] (deg)	ϖ	134 ± 23
Derived parameters		
Standard gravitational parameter GM_{sys} (km^3 s^{-2})	μ	32.85 ± 0.47
System mass (10^{18} kg)	M_{sys}	492.2 ± 7.1
Orbit pole right ascension[b] (deg)	α_{pole}	315.2 ± 1.4
Orbit pole declination[b] (deg)	δ_{pole}	66.42 ± 0.36
Orbit pole ecliptic longitude[d] (deg)	λ_{pole}	20.4 ± 1.6
Orbit pole ecliptic latitude[d] (deg)	β_{pole}	72.36 ± 0.46
Inclination to heliocentric orbit (deg)		41.35 ± 0.43
Next mutual events season (year)		2110

Table notes:

[a.] Elements are for Actaea relative to Salacia. Excluding two low precision NIRI observations, the average sky plane residual for Orbit 1 is 7 mas and the maximum is 18 mas; χ^2 is 52, based on observations at 14 epochs. This value of χ^2 suggests the orbit solution can be excluded at 3.7 σ confidence, implying potential problems with some of the astrometric data or their uncertainties, or with the assumption of purely Keplerian motion. The mirror orbit solution has a much worse χ^2 = 137, allowing us to exclude it, albeit subject to the possibility of faulty astrometric data.

[b.] Referenced to J2000 equatorial frame.

[c.] The epoch is Julian date 2454300, corresponding to 2007 July 18 12:00 UT.

[d.] Referenced to J2000 ecliptic frame.

Table 6

Orbit solutions and 1-σ uncertainties for 160091 2000 OL_{67} and its satellite

Parameter		Orbit 1 value	Orbit 2 value
Fitted elements[a]		$\chi^2 = 7.6$	$\chi^2 = 15$
Period (days)	P	346.89 ± 0.19	347.28 ± 0.28
Semimajor axis (km)	a	7560 ± 210	7830 ± 550
Eccentricity	e	0.220 ± 0.022	0.253 ± 0.018
Inclination[b] (deg)	i	80.6 ± 4.2	93.5 ± 7.2
Mean longitude[b] at epoch[c] (deg)	ϵ	333.1 ± 3.6	25.8 ± 4.8
Longitude of asc. node[b] (deg)	Ω	226.2 ± 3.5	286.8 ± 6.4
Longitude of periapsis[b] (deg)	ϖ	248.5 ± 3.6	300.5 ± 7.0
Derived parameters			
Standard gravitational parameter GM_{sys} ($km^3\ s^{-2}$)	μ	0.0190 ± 0.0016	0.0211 ± 0.0051
System mass (10^{18} kg)	M_{sys}	0.285 ± 0.024	0.316 ± 0.076
Orbit pole right ascension[b] (deg)	α_{pole}	136.2 ± 3.5	196.8 ± 5.9
Orbit pole declination[b] (deg)	δ_{pole}	9.4 ± 4.3	−3.5 ± 6.9
Orbit pole ecliptic longitude[d] (deg)	λ_{pole}	135.9 ± 3.5	196.8 ± 4.3
Orbit pole ecliptic latitude[d] (deg)	β_{pole}	−7.0 ± 4.2	3.4 ± 7.7
Inclination to heliocentric orbit (deg)		97.0 ± 4.1	83.9 ± 8.6
Next mutual events season (year)		2059	2121

Table notes:

[a.] Elements are for secondary relative to primary. Excluding two low precision NIRI observations, the average sky plane residual for Orbit 1 is 4.5 mas and the maximum is 9 mas. For Orbit 2 the average residual is 10 mas.

[b.] Referenced to J2000 equatorial frame.

[c.] The epoch is Julian date 2457000, corresponding to 2014 December 8 12:00 UTC.

[d.] Referenced to J2000 ecliptic frame.

Table 7

Orbit solution and 1-σ uncertainties for 160256 2002 PD_{149} and its satellite

Parameter		Value
Fitted elements[a]		
Period (days)	P	1675.5 ± 3.2
Semimajor axis (km)	a	26780 ± 340
Eccentricity	e	0.5879 ± 0.0083
Inclination[b] (deg)	i	32.92 ± 0.39
Mean longitude[b] at epoch[c] (deg)	ϵ	58.49 ± 0.77
Longitude of asc. node[b] (deg)	Ω	55.29 ± 1.0
Longitude of periapsis[b] (deg)	ϖ	246.8 ± 2.1
Derived parameters		
Standard gravitational parameter GM_{sys} (km^3 s^{-2})	μ	0.0362 ± 0.0015
System mass (10^{18} kg)	M_{sys}	0.542 ± 0.022
Orbit pole right ascension[b] (deg)	α_{pole}	325.3 ± 1.0
Orbit pole declination[b] (deg)	δ_{pole}	57.08 ± 0.39
Orbit pole ecliptic longitude[d] (deg)	λ_{pole}	6.4 ± 1.1
Orbit pole ecliptic latitude[d] (deg)	β_{pole}	63.29 ± 0.48
Inclination to heliocentric orbit (deg)		21.89 ± 0.48
Next mutual events season (year)		2088

Table notes:

[a.] Elements are for secondary relative to primary. The average sky plane residual for the orbit solution is 8 mas and the maximum is 35 mas; χ^2 is 1.14, based on observations at 5 epochs. For the mirror orbit solution, χ^2 is 208, allowing us to exclude it with > 6 σ confidence.

[b.] Referenced to J2000 equatorial frame.

[c.] The epoch is Julian date 2457000, corresponding to 2014 December 8 12:00 UTC.

[d.] Referenced to J2000 ecliptic frame.

Table 8

Orbit solutions and 1-σ uncertainties for 469514 2003 QA_{91} and its satellite

Parameter		Orbit 1 value	Orbit 2 value
Fitted elements[a]		$\chi^2 = 27.3$	$\chi^2 = 27.7$
Period (days)	P	10.10884 ± 0.00020	10.10897 ± 0.00021
Semimajor axis (km)	a	1598 ± 40	1590 ± 40
Eccentricity	e	0.027 ± 0.016	0.019 ± 0.014
Inclination[b] (deg)	i	88.0 ± 8.4	111 ± 11
Mean longitude[b] at epoch[c] (deg)	ϵ	217.0 ± 9.1	207 ± 10
Longitude of asc. node[b] (deg)	Ω	67.5 ± 8.6	60.2 ± 7.5
Longitude of periapsis[b] (deg)	ϖ	290 ± 43	265 ± 58
Derived parameters			
Standard gravitational parameter GM_{sys} ($km^3\ s^{-2}$)	μ	0.211 ± 0.016	0.208 ± 0.016
System mass (10^{18} kg)	M_{sys}	3.16 ± 0.24	3.11 ± 0.24
Orbit pole right ascension[b] (deg)	α_{pole}	337.5 ± 8.7	330.2 ± 7.1
Orbit pole declination[b] (deg)	δ_{pole}	2.0 ± 7.7	−21 ± 10
Orbit pole ecliptic longitude[d] (deg)	λ_{pole}	339.9 ± 9.2	324.8 ± 1.6
Orbit pole ecliptic latitude[d] (deg)	β_{pole}	10.6 ± 7.4	−9 ± 10
Inclination to heliocentric orbit (deg)		77.3 ± 7.7	96 ± 11
Next mutual events season (year)		2083	2072

Table notes:

[a.] Elements are for secondary relative to primary. The average sky plane residual for Orbit 1 is 3.5 mas and the maximum is 11 mas. For Orbit 2 the average residual is 3.6 mas.

[b.] Referenced to J2000 equatorial frame.

[c.] The epoch is Julian date 2457000, corresponding to 2014 December 8 12:00 UTC.

[d.] Referenced to J2000 ecliptic frame.

Table 9

Orbit solution and 1-σ uncertainties for 469705 ǂKágára and its satellite !Hãunu

Parameter		Value
Fitted elements[a]		
Period (days)	P	128.107 ± 0.027
Semimajor axis (km)	a	7670 ± 140
Eccentricity	e	0.694 ± 0.013
Inclination[b] (deg)	i	33.33 ± 0.41
Mean longitude[b] at epoch[c] (deg)	ϵ	136.08 ± 0.88
Longitude of asc. node[b] (deg)	Ω	4.13 ± 0.32
Longitude of periapsis[b] (deg)	ϖ	183.57 ± 0.76
Derived parameters		
Standard gravitational parameter GM_{sys} (km^3 s^{-2})	μ	0.1455 ± 0.0080
System mass (10^{18} kg)	M_{sys}	2.18 ± 0.12
Orbit pole right ascension[b] (deg)	α_{pole}	274.13 ± 0.33
Orbit pole declination[b] (deg)	δ_{pole}	56.67 ± 0.42
Orbit pole ecliptic longitude[d] (deg)	λ_{pole}	283.1 ± 1.1
Orbit pole ecliptic latitude[d] (deg)	β_{pole}	79.92 ± 0.41
Inclination to heliocentric orbit (deg)		11.17 ± 0.41
Next mutual events season (year)		2025

Table notes:

[a.] Elements are for !Hãunu relative to ǂKágára. The average sky plane residual for the orbit solution is 8 mas and the maximum is 43 mas; χ^2 is 23.4, based on observations at 10 epochs. For the mirror orbit solution, χ^2 is 67, allowing us to exclude it with 5.9 σ confidence.

[b.] Referenced to J2000 equatorial frame.

[c.] The epoch is Julian date 2455600, corresponding to 2011 February 7 12:00 UTC.

[d.] Referenced to J2000 ecliptic frame.

Table 10

Orbit solution and 1-σ uncertainties for 508788 2000 CQ_{114} and its satellite

Parameter		Value
Fitted elements[a]		
Period (days)	P	220.478 ± 0.045
Semimajor axis (km)	a	6940 ± 32
Eccentricity	e	0.0950 ± 0.0047
Inclination[b] (deg)	i	32.13 ± 0.56
Mean longitude[b] at epoch[c] (deg)	ϵ	62.31 ± 0.66
Longitude of asc. node[b] (deg)	Ω	106.28 ± 0.68
Longitude of periapsis[b] (deg)	ϖ	113.2 ± 3.7
Derived parameters		
Standard gravitational parameter GM_{sys} (km^3 s^{-2})	μ	0.03637 ± 0.00051
System mass (10^{18} kg)	M_{sys}	0.5449 ± 0.0076
Orbit pole right ascension[b] (deg)	α_{pole}	16.28 ± 0.69
Orbit pole declination[b] (deg)	δ_{pole}	57.87 ± 0.57
Orbit pole ecliptic longitude[d] (deg)	λ_{pole}	42.85 ± 0.76
Orbit pole ecliptic latitude[d] (deg)	β_{pole}	45.86 ± 0.41
Inclination to heliocentric orbit (deg)		44.40 ± 0.40
Next mutual events season (year)		2160

Table notes:

[a.] Elements are for secondary relative to primary. The average sky plane residual for the orbit solution is 0.9 mas and the maximum is 1.7 mas; χ^2 is 1.0, based on observations at 7 epochs. For the mirror orbit solution, χ^2 is 74, allowing us to exclude it with > 6 σ confidence.

[b.] Referenced to J2000 equatorial frame.

[c.] The epoch is Julian date 2454100, corresponding to 2006 December 30 12:00 UTC.

[d.] Referenced to J2000 ecliptic frame.

Table 11

Orbit solutions and 1-σ uncertainties for 508869 2002 VT_{130} and its satellite

Parameter		Orbit 1 value	Orbit 2 value
Fitted elements[a]		$\chi^2 = 8.8$	$\chi^2 = 9.3$
Period (days)	P	30.7577 ± 0.0026	30.7656 ± 0.0023
Semimajor axis (km)	a	3042 ± 74	3004 ± 68
Eccentricity	e	0.0187 ± 0.0082	0.0195 ± 0.0062
Inclination[b] (deg)	i	52.6 ± 2.8	88.4 ± 2.8
Mean longitudeb at epoch[c] (deg)	ϵ	85.9 ± 1.3	129.7 ± 2.1
Longitude of asc. node[b] (deg)	Ω	115.4 ± 2.6	191.0 ± 2.2
Longitude of periapsis[b] (deg)	ϖ	149 ± 31	262 ± 28
Derived parameters			
Standard gravitational parameter GM_{sys} (km^3 s^{-2})	μ	0.157 ± 0.012	0.151 ± 0.010
System mass (10^{18} kg)	M_{sys}	2.36 ± 0.17	2.27 ± 0.16
Orbit pole right ascension[b] (deg)	α_{pole}	25.4 ± 2.5	101.0 ± 2.3
Orbit pole declination[b] (deg)	δ_{pole}	37.4 ± 2.8	1.6 ± 2.9
Orbit pole ecliptic longitude[d] (deg)	λ_{pole}	37.7 ± 2.4	101.8 ± 2.3
Orbit pole ecliptic latitude[d] (deg)	β_{pole}	25.0 ± 2.8	−21.4 ± 3.1
Inclination to heliocentric orbit (deg)		66.1 ± 2.7	112.4 ± 2.9
Next mutual events season (year)		2156	2109

Table notes:

[a.] Elements are for secondary relative to primary. The average sky plane residual for Orbit 1 is 2.5 mas and the maximum is 4.7 mas. For Orbit 2 the average residual is 2.0 mas.

[b.] Referenced to J2000 equatorial frame.

[c.] The epoch is Julian date 2455900, corresponding to 2011 December 4 12:00 UTC.

[d.] Referenced to J2000 ecliptic frame.

Table 12

Orbit solution and 1-σ uncertainties for 1998 WW_{31} and its satellite

Parameter		Value
Fitted elements[a]		
Period (days)	P	587.27 ± 0.18
Semimajor axis (km)	a	22617 ± 42
Eccentricity	e	0.8193 ± 0.0020
Inclination[b] (deg)	i	41.36 ± 0.38
Mean longitude[b] at epoch[c] (deg)	ϵ	30.83 ± 0.34
Longitude of asc. node[b] (deg)	Ω	94.58 ± 0.72
Longitude of periapsis[b] (deg)	ϖ	348.49 ± 0.63
Derived parameters		
Standard gravitational parameter GM_{sys} (km^3 s^{-2})	μ	0.17739 ± 0.00097
System mass (10^{18} kg)	M_{sys}	2.658 ± 0.015
Orbit pole right ascension[b] (deg)	α_{pole}	4.58 ± 0.72
Orbit pole declination[b] (deg)	δ_{pole}	48.64 ± 0.38
Orbit pole ecliptic longitude[d] (deg)	λ_{pole}	27.77 ± 0.62
Orbit pole ecliptic latitude[d] (deg)	β_{pole}	41.88 ± 0.41
Inclination to heliocentric orbit (deg)		51.71 ± 0.40
Next mutual events season (year)		2055

Table notes:

[a.] Elements are for secondary relative to primary. The average sky plane residual for the orbit solution is 7 mas and the maximum is 43 mas; χ^2 is 26.2, based on observations at 16 epochs. For the mirror orbit solution, χ^2 is 55, allowing us to exclude it with 3.5 σ confidence.

[b.] Referenced to J2000 equatorial frame.

[c.] The epoch is Julian date 2452300, corresponding to 2002 January 25 12:00 UTC.

[d.] Referenced to J2000 ecliptic frame.

Table 13

Orbit solution and 1-σ uncertainties for 1999 OJ_4 and its satellite

Parameter		Value
Fitted elements[a]		
Period (days)	P	84.1147 ± 0.0050
Semimajor axis (km)	a	3306 ± 17
Eccentricity	e	0.3683 ± 0.0038
Inclination[b] (deg)	i	53.61 ± 0.72
Mean longitude[b] at epoch[c] (deg)	ϵ	37.45 ± 0.90
Longitude of asc. node[b] (deg)	Ω	276.0 ± 1.3
Longitude of periapsis[b] (deg)	ϖ	330.2 ± 0.61
Derived parameters		
Standard gravitational parameter GM_{sys} (km^3 s^{-2})	μ	0.02700 ± 0.00042
System mass (10^{18} kg)	M_{sys}	0.4045 ± 0.0063
Orbit pole right ascension[b] (deg)	α_{pole}	186.1 ± 1.3
Orbit pole declination[b] (deg)	δ_{pole}	36.39 ± 0.72
Orbit pole ecliptic longitude[d] (deg)	λ_{pole}	168.8 ± 1.1
Orbit pole ecliptic latitude[d] (deg)	β_{pole}	35.31 ± 0.88
Inclination to heliocentric orbit (deg)		57.36 ± 0.83
Next mutual events season (year)		2078

Table notes:

[a.] Elements are for secondary relative to primary. Excluding low precision NICMOS and NIRI observations, the average sky plane residual for the orbit solution is 3 mas and the maximum is 10 mas; χ^2 is 13.8, based on observations at 10 epochs. For the mirror orbit solution, χ^2 is 39, allowing us to exclude it with 3.7 σ confidence.

[b.] Referenced to J2000 equatorial frame.

[c.] The epoch is Julian date 2454000, corresponding to 2006 September 21 12:00 UTC.

[d.] Referenced to J2000 ecliptic frame.

Table 14

Orbit solution and 1-σ uncertainties for 1999 RT_{214} and its satellite

Parameter		Value
Fitted elements[a]		
Period (days)	P	126.504 ± 0.046
Semimajor axis (km)	a	3396 ± 66
Eccentricity	e	0.298 ± 0.026
Inclination[b] (deg)	i	37.5 ± 1.2
Mean longitude[b] at epoch[c] (deg)	ϵ	125.7 ± 1.9
Longitude of asc. node[b] (deg)	Ω	40.1 ± 2.1
Longitude of periapsis[b] (deg)	ϖ	156.8 ± 1.9
Derived parameters		
Standard gravitational parameter GM_{sys} (km^3 s^{-2})	μ	0.01294 ± 0.00074
System mass (10^{18} kg)	M_{sys}	0.194 ± 0.011
Orbit pole right ascension[b] (deg)	α_{pole}	310.1 ± 2.2
Orbit pole declination[b] (deg)	δ_{pole}	52.5 ± 1.3
Orbit pole ecliptic longitude[d] (deg)	λ_{pole}	344.0 ± 2.7
Orbit pole ecliptic latitude[d] (deg)	β_{pole}	65.9 ± 1.5
Inclination to heliocentric orbit (deg)		22.6 ± 1.4
Next mutual events season (year)		2078

Table notes:

[a.] Elements are for secondary relative to primary. The average sky plane residual for the orbit solution is 5 mas and the maximum is 10 mas; χ^2 is 17.5, based on observations at 6 epochs. For the mirror orbit solution χ^2 is 52, allowing us to exclude it with > 6 σ confidence.

[b.] Referenced to J2000 equatorial frame.

[c.] The epoch is Julian date 2457000, corresponding to 2014 December 8 12:00 UTC.

[d.] Referenced to J2000 ecliptic frame.

Table 15

Orbit solution and 1-σ uncertainties for 2000 QL_{251} and its satellite

Parameter		Value
Fitted elements[a]		
Period (days)	P	56.4495 ± 0.0039
Semimajor axis (km)	a	4992 ± 16
Eccentricity	e	0.4893 ± 0.0040
Inclination[b] (deg)	i	127.69 ± 0.57
Mean longitude[b] at epoch[c] (deg)	ϵ	145.6 ± 1.0
Longitude of asc. node[b] (deg)	Ω	109.24 ± 0.81
Longitude of periapsis[b] (deg)	ϖ	151.66 ± 0.94
Derived parameters		
Standard gravitational parameter GM_{sys} (km^3 s^{-2})	μ	0.2065 ± 0.0019
System mass (10^{18} kg)	M_{sys}	3.094 ± 0.029
Orbit pole right ascension[b] (deg)	α_{pole}	19.24 ± 0.82
Orbit pole declination[b] (deg)	δ_{pole}	−37.69 ± 0.57
Orbit pole ecliptic longitude[d] (deg)	λ_{pole}	359.70 ± 0.86
Orbit pole ecliptic latitude[d] (deg)	β_{pole}	−41.66 ± 0.60
Inclination to heliocentric orbit (deg)		134.14 ± 0.58
Next mutual events season (year)		2084

Table notes:

[a.] Elements are for secondary relative to primary. The average sky plane residual for the orbit solution is 2.2 mas and the maximum is 10 mas; χ^2 is 3.6, based on observations at 10 epochs. For the mirror orbit solution, χ^2 is 38.2, allowing us to exclude it with 3.6 σ confidence.

[b.] Referenced to J2000 equatorial frame.

[c.] The epoch is Julian date 2454200, corresponding to 2007 April 9 12:00 UTC.

[d.] Referenced to J2000 ecliptic frame.

Table 16

Orbit solution and 1-σ uncertainties for 2001 XR_{254} and its satellite

Parameter		Value
Fitted elements[a]		
Period (days)	P	125.579 ± 0.048
Semimajor axis (km)	a	9311 ± 52
Eccentricity	e	0.5561 ± 0.0047
Inclination[b] (deg)	i	41.08 ± 0.22
Mean longitude[b] at epoch[c] (deg)	ϵ	151.97 ± 0.29
Longitude of asc. node[b] (deg)	Ω	341.19 ± 0.29
Longitude of periapsis[b] (deg)	ϖ	246.29 ± 0.93
Derived parameters		
Standard gravitational parameter GM_{sys} (km^3 s^{-2})	μ	0.2707 ± 0.0044
System mass (10^{18} kg)	M_{sys}	4.055 ± 0.048
Orbit pole right ascension[b] (deg)	α_{pole}	251.19 ± 0.29
Orbit pole declination[b] (deg)	δ_{pole}	48.92 ± 0.22
Orbit pole ecliptic longitude[d] (deg)	λ_{pole}	231.96 ± 0.53
Orbit pole ecliptic latitude[d] (deg)	β_{pole}	69.88 ± 0.23
Inclination to heliocentric orbit (deg)		21.10 ± 0.23
Next mutual events season (year)		2037

Table notes:

[a.] Elements are for secondary relative to primary. The average sky plane residual for the orbit solution is 1.9 mas and the maximum is 3.5 mas; χ^2 is 6.3, based on observations at 8 epochs. For the mirror orbit solution, χ^2 is 44, allowing us to exclude it with 4.8 σ confidence.

[b.] Referenced to J2000 equatorial frame.

[c.] The epoch is Julian date 2454300, corresponding to 2007 July 18 12:00 UTC.

[d.] Referenced to J2000 ecliptic frame.

Table 17

Orbit solution and 1-σ uncertainties for 2002 XH_{91} and its satellite

Parameter		Value
Fitted elements[a]		
Period (days)	P	371.15 ± 0.17
Semimajor axis (km)	a	22430 ± 410
Eccentricity	e	0.715 ± 0.015
Inclination[b] (deg)	i	29.2 ± 1.7
Mean longitude[b] at epoch[c] (deg)	ϵ	274.1 ± 2.7
Longitude of asc. node[b] (deg)	Ω	278.0 ± 1.8
Longitude of periapsis[b] (deg)	ϖ	69.7 ± 1.0
Derived parameters		
Standard gravitational parameter GM_{sys} (km^3 s^{-2})	μ	0.433 ± 0.024
System mass (10^{18} kg)	M_{sys}	6.49 ± 0.36
Orbit pole right ascension[b] (deg)	α_{pole}	188.0 ± 1.8
Orbit pole declination[b] (deg)	δ_{pole}	60.8 ± 1.7
Orbit pole ecliptic longitude[d] (deg)	λ_{pole}	149.4 ± 2.1
Orbit pole ecliptic latitude[d] (deg)	β_{pole}	55.9 ± 1.5
Inclination to heliocentric orbit (deg)		38.7 ± 1.5
Next mutual events season (year)		2118

Table notes:

[a.] Elements are for secondary relative to primary. The average sky plane residual for the orbit solution is 6.6 mas and the maximum is 24 mas; χ^2 is 5.1, based on observations at 5 epochs. For the mirror orbit solution, χ^2 is 780, allowing us to exclude it with > 6 σ confidence.

[b.] Referenced to J2000 equatorial frame.

[c.] The epoch is Julian date 2457000, corresponding to 2014 December 8 12:00 UT.

[d.] Referenced to J2000 ecliptic frame.

Table 18

Orbit solution and 1-σ uncertainties for 2003 TJ_{58} and its satellite

Parameter		Value
Fitted elements[a]		
Period (days)	P	137.682 ± 0.034
Semimajor axis (km)	a	3834 ± 50
Eccentricity	e	0.5162 ± 0.0083
Inclination[b] (deg)	i	39.3 ± 1.9
Mean longitude[b] at epoch[c] (deg)	ϵ	58.3 ± 1.9
Longitude of asc. node[b] (deg)	Ω	198.6 ± 3.4
Longitude of periapsis[b] (deg)	ϖ	85.01 ± 0.74
Derived parameters		
Standard gravitational parameter GM_{sys} (km^3 s^{-2})	μ	0.01573 ± 0.00061
System mass (10^{18} kg)	M_{sys}	0.2356 ± 0.0092
Orbit pole right ascension[b] (deg)	α_{pole}	108.6 ± 3.3
Orbit pole declination[b] (deg)	δ_{pole}	50.7 ± 1.9
Orbit pole ecliptic longitude[d] (deg)	λ_{pole}	103.2 ± 2.4
Orbit pole ecliptic latitude[d] (deg)	β_{pole}	28.1 ± 1.9
Inclination to heliocentric orbit (deg)		62.8 ± 1.9
Next mutual events season (year)		2101

Table notes:

[a.] Elements are for secondary relative to primary. The average sky plane residual for the orbit solution is 2.4 mas and the maximum is 4.8 mas; χ^2 is 8.0, based on observations at 6 epochs. For the mirror orbit solution, χ^2 is 34, allowing us to exclude it with 4.7 σ confidence.

[b.] Referenced to J2000 equatorial frame.

[c.] The epoch is Julian date 2454300, corresponding to 2007 July 18 12:00 UTC.

[d.] Referenced to J2000 ecliptic frame.

Table 19

Mutual and heliocentric orbital properties of transneptunian binaries

	Mutual orbit			Heliocentric orbit[b]							
Object[a]	*P* (days)	*a* (km)	*e*	H_V (mags)	Δ_{mag} (mags)	atan(*a*/*r*) (arcsec)	$\langle a_\odot \rangle$ (AU)	$\langle e_\odot \rangle$	$\langle i_\odot \rangle$ (deg)	a/r_H	Incl.[c] (deg)
26308 1998 SM_{165}	130.154	11374	0.4732	6.1	2.7	0.38	47.8	0.37	13.14	0.024	75.5
42355 Typhon	18.9815	1580	0.507	7.7	1.3	0.10	37.3	0.53	3.75	0.012	53.4
50000 Quaoar	12.431	13330	0.021	2.7	5.6	0.43	43.4	0.04	8.52	0.004	-
55637 2002 UX_{25}	8.3095	4750	0.18	3.9	2.5	0.16	42.7	0.14	20.23	0.003	65.0
58534 Logos	309.9	8220	0.546	7.3	0.5	0.26	45.3	0.13	2.01	0.033	74.2
60458 2000 CM_{114}	24.825	2500	0.03	7.4	0.6	0.09	59.6	0.40	21.70	0.007	55.5
65489 Ceto	9.560	1850	0.008	6.6	0.6	0.06	100.7	0.82	21.51	0.007	-
66652 Borasisi	46.289	4530	0.470	6.0	0.5	0.15	43.7	0.09	1.62	0.009	49.4
79360 Sila-Nunam	12.51006	2770	0.026	5.5	0.1	0.09	43.9	0.01	3.84	0.004	123.2
88611 Teharonhiawako	828.8	27600	0.249	6.1	0.7	0.84	44.1	0.03	4.18	0.058	127.6
90482 Orcus	9.53915	9000	0.0009	2.3	2.6	0.26	39.5	0.25	21.19	0.004	106.6
119979 2002 WC_{19}	8.403	4090	0.20	5.0	3.1	0.14	47.8	0.26	7.67	0.003	-
120347 Salacia	5.49388	5720	0.010	4.2	2.4	0.18	42.1	0.10	25.57	0.002	41.4
123509 2000 WK_{183}	30.913	2370	0.014	6.7	0.1	0.08	44.4	0.05	2.72	0.007	-
134860 2000 OJ_{67}	22.0585	2270	0.012	6.5	0.6	0.07	42.9	0.01	1.32	0.005	-
136199 Eris	15.78590	37270	0.0062	−1.2	6.7	0.54	67.9	0.45	43.21	0.005	78.4
148780 Altjira	139.56	9900	0.344	6.3	0.2	0.30	44.3	0.06	5.47	0.018	25.4
160091 2000 OL_{67}	347.1	7800	0.24	7.1	0.6	0.24	45.2	0.11	3.49	0.035	-
160256 2002 PD_{149}	1675	26800	0.588	6.6	0.4	0.83	43.0	0.07	3.30	0.099	21.9
174567 Varda	5.7506	4810	0.022	3.6	1.5	0.14	45.8	0.15	21.24	0.002	-
229762 G!kúnǁ'hòmdímà	11.3147	6040	0.024	3.7	3.8	0.20	73.7	0.49	21.84	0.004	32.2
275809 2001 QY_{297}	138.118	9960	0.418	5.9	0.2	0.31	43.9	0.07	0.96	0.019	161.0
341520 Mors-Somnus	972.2	20990	0.1494	6.9	0.1	1.00	39.5	0.27	11.54	0.096	24.3
364171 2006 JZ_{81}	1500	33000	0.85	7.0	1.0	1.11	44.8	0.08	2.99	0.090	11.0
385446 Manwë	110.18	6670	0.563	7.4	1.2	0.21	43.7	0.11	1.14	0.017	49.1
469514 2003 QA_{91}	10.1089	1590	0.02	5.9	0.1	0.05	44.4	0.08	1.04	0.003	-
469705 ǂKágára	128.11	7700	0.69	6.2	0.6	0.26	44.1	0.09	1.60	0.018	11.2
508788 2000 CQ_{114}	220.48	6940	0.095	7.2	0.1	0.20	46.2	0.12	2.20	0.025	44.4
508869 2002 VT_{130}	30.761	3030	0.019	6.0	0.4	0.10	42.5	0.03	2.78	0.007	-
1998 WW_{31}	587.3	22620	0.819	6.5	0.4	0.65	44.7	0.09	8.34	0.048	51.7
1999 OJ_4	84.115	3310	0.368	7.3	0.1	0.12	38.1	0.02	2.59	0.014	57.4
1999 RT_{214}	126.50	3400	0.30	8.1	1.0	0.12	42.6	0.06	2.78	0.018	23.1
2000 CF_{105}	3900	34300	0.33	8.0	0.7	1.11	43.9	0.04	1.36	0.165	-
2000 QL_{251}	56.449	4990	0.489	7.1	0.1	0.17	47.8	0.21	5.83	0.011	134.1
2001 QC_{298}	19.2287	3810	0.334	6.6	0.4	0.13	46.3	0.13	31.54	0.005	73.7
2001 QW_{322}	6280	102100	0.464	8.1	0.0	3.16	44.1	0.02	3.50	0.223	152.8
2001 XR_{254}	125.58	9310	0.556	6.0	0.4	0.29	43.0	0.02	2.66	0.017	21.1
2002 XH_{91}	371.1	22400	0.71	5.8	1.0	0.66	44.0	0.08	3.04	0.036	38.8

2003 QY_{90}	309.6	8550	0.663	6.9	0.0	0.26	42.8	0.06	2.21	0.032	51.4
2003 TJ_{58}	137.68	3830	0.516	7.4	0.5	0.13	44.5	0.09	1.31	0.019	62.7
2003 UN_{284}	3180	54000	0.38	7.7	0.9	1.77	42.7	0.02	2.11	0.145	23.0
2004 PB_{108}	97.020	10400	0.438	7.0	1.3	0.34	45.2	0.11	19.19	0.015	83.2
2005 EO_{304}	3580	70000	0.22	6.4	1.5	2.23	45.7	0.06	1.68	0.154	15.9
2006 BR_{284}	1501	25400	0.275	7.2	0.5	0.83	43.9	0.05	1.81	0.088	54.1
2006 CH_{69}	1420	27000	0.896	7.1	0.4	0.84	45.8	0.04	1.58	0.081	132.5

Table notes:

[a.] Objects in bold font are those with new information presented in this paper. Previously published orbits are from Brown & Schaller (2007), Grundy et al. (2009, 2011), Parker et al. (2011), Sheppard et al. (2012), Grundy et al. (2014, 2015), Brown & Butler (2017), and Grundy et al. (2019).

[b.] Mean values averaged over 10 Myr orbital integrations.

[c.] Inclination between the mutual orbit and the heliocentric orbit. Systems with ambiguous inclinations are indicated with a dash.